



**AALBORG UNIVERSITY**

STUDENT REPORT

DESIGN OF MECHANICAL SYSTEMS

MASTER'S THESIS

---

# Dynamic Analysis of Compliant Joint for Assistive Exoskeleton

---



*Participant*

Elizabeth Napoleon Paul

*Supervisor*

Shaoping Bai

---



**AALBORG UNIVERSITY**  
STUDENT REPORT

**4th semester - School of  
Engineering and Science**  
Design of Mechanical Systems  
Fibigerstræde 16  
9220 Aalborg East  
<http://www.ses.aau.dk>

**Title:**

Master's Thesis

**Theme:**

Engineering Design of Mechanical Systems

**Project period:**

February 3rd - June 3rd, 2020

**Project group:**

14-23E

**Participant:**

Elizabeth Napoleon Paul

**Supervisor:**

Shaoping Bai

**Examiner:**

Xuping Zhang

**Page numbers:** 55

**Appendix enclosures:** 2

**Date of completion:** June 3rd, 2020

**Abstract:**

This project investigates the nonlinear dynamic analysis of a compliant joint for an assistive exoskeleton. The compliant mechanism was modeled as a 1 DOF pendulum system and a dynamic model was obtained using Lagrangian formulation. The numerical Runge-Kutta and analytical Harmonic balance method (HBM) were utilized in solving the dynamic equation. Both methods were used to show the chaotic and jump phenomenon behaviors associated with the nonlinear dynamic model. Subsequently, the model was validated by running simulations in MSC Adams and comparing the solution with Runge-Kutta method. The results showed a good correlation with errors ranging between 0 and  $0.09rad$ . Afterward, HBM and Runge-Kutta were compared and the results matched closely with an error between  $\pm 0.008rad$ . Finally, the dynamic model was further extended to include an actuator. Series elastic (SEA) and Parallel elastic (PEA) actuators were considered. Power analysis for both PEA and SEA was done using inverse dynamics analysis and the results showed that an increase in stiffness from softening to hardening reduces the power requirement of the system.

# Preface

This thesis is for the 4th semester of Master degree in Design of Mechanical Systems offered at Aalborg University, Denmark. The thesis period was from the 1st of February to the 3rd, of June 2020. It investigates the nonlinear dynamic analysis of a compliant joint mechanism. The author appreciates Shaoping Bai, Professor at Aalborg University, who supervised this project. The author would also like to appreciate Zhongyi Li, for providing CAD model and insight on the compliant mechanism. Finally, thanks go to Dr. Simeon Onyemaechi for proofreading the report.

## Reading guide

The source referencing of this report is done using the Harvard method [Surname, year]. The complete list of literature can be found at the end of the report. The figures, tables and equations in the report are itemized according to the format of (a,b), where a represents the chapter number where the figure is placed and b represents the order of the figures, tables and equations. The appendices are designated by a letter and the sections are itemized as in the main report.

The following software are used in the project

- MatLab R2019a
- MSC Adams/View
- Excel
- Inkscape
- SolidWorks

# Table of contents

<b>Preface</b>	<b>III</b>
<b>Table of contents</b>	<b>IV</b>
<b>Chapter 1 Introduction</b>	<b>1</b>
1.1 Project Scope . . . . .	2
<b>Chapter 2 Nonlinear Dynamic Model</b>	<b>3</b>
2.1 The compliant joint kinematics . . . . .	3
2.2 Dynamics . . . . .	5
2.3 Methods . . . . .	6
2.4 Joint dynamic model . . . . .	6
<b>Chapter 3 Methods</b>	<b>9</b>
3.1 The harmonic balance method . . . . .	9
3.2 Runge-Kutta method . . . . .	12
3.3 MSC Adams simulation . . . . .	14
3.4 Preliminary results . . . . .	17
3.5 Dynamic response . . . . .	19
3.6 Nonlinear behaviors . . . . .	20
<b>Chapter 4 Compliant Joint Dynamics</b>	<b>23</b>
4.1 Results and discussion . . . . .	24
<b>Chapter 5 Model Validation</b>	<b>33</b>
5.1 Determining damping coefficient . . . . .	33
5.2 Runge-Kutta vs Adams . . . . .	34
5.3 Harmonic Balance Method Vs. Runge-Kutta . . . . .	36
<b>Chapter 6 Extended Model Dynamics</b>	<b>39</b>
6.1 Actuators . . . . .	39
6.2 Dynamic model . . . . .	40
6.3 Dynamic analysis . . . . .	41
6.4 Power analysis . . . . .	44

<b>Chapter 7 Conclusion</b>	<b>47</b>
7.1 Further Work . . . . .	48
<b>Bibliography</b>	<b>49</b>
<b>A Trigonometric Identities</b>	<b>53</b>
<b>B Data Sheet</b>	<b>55</b>



# 1 | Introduction

The exoskeleton is a human-robot interaction system that augments the operator's ability in various environments. It has been widely used in the medical, rehabilitation, haptic interaction and power-assisted fields.

This thesis is a part of an ongoing research and development InnovationsFonden project on assistive exoskeleton called Exo-aider. Exo-aider's objective is to develop end-user driven innovations in assistive exoskeleton technology to meet the growing needs of motion assistance of elderly people and individuals with physical disabilities. Shown in Fig. 1.1 is the current upper-body exoskeleton at Alborg University (AAU).

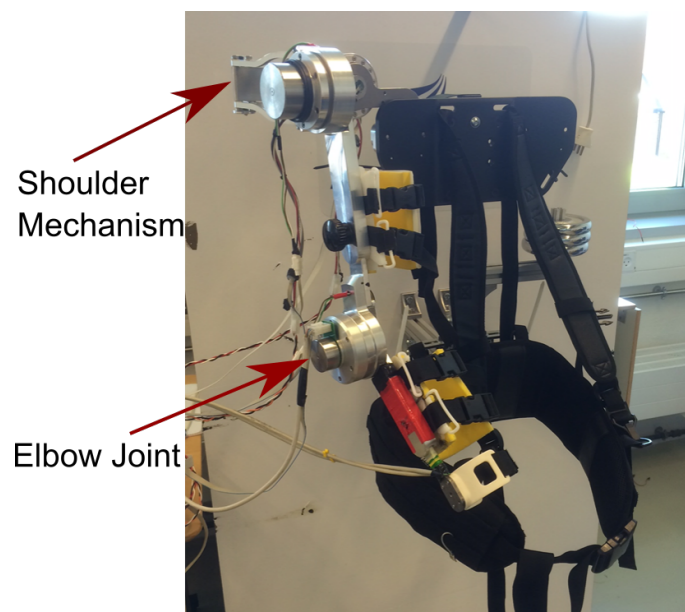


Figure 1.1: Upper-body exoskeleton Bai et al. [2017]

One of the major considerations with exoskeletons is the human-robotic interaction in terms of safety, dexterity, flexibility and compatibility. As a part of Exo-aider's project, Bai et al. [2017] designed and successfully tested the human-robotic interaction of the shoulder mechanism. It is a novel spherical mechanism that consists of two revolute joints connected together via a double parallelogram linkage. It allows for spherical motion of the exoskeleton that is comparable to that of the human arm [Bai et al., 2017]. The elbow mechanism is a single powered joint that supports flexion/extension of the human elbow [Christensen et al., 2019].

Another milestone in the research is a novel revolute compliant joint mechanism [Li and Bai, 2019]. Compliant joints are used to increase the safety of physical human-robotic interaction, enhance the energy efficiency and improve the dynamic adaptability to the environment. The implementation of this compliant joint mechanism into the exoskeleton's elbow joint is considered in this project.

## 1.1 Project Scope

The scope of this project is the dynamic modeling and analysis of the compliant joint. In exoskeleton design, there exist many critical design problems which include kinematic considerations, joint range of motion, degrees of freedom, torque and velocity requirements for joints, weight and inertia, etc. However, the most crucial issue is dynamics and corresponding system control and balancing methodologies [Yan et al., 2019]

### 1.1.1 Project objective

The objective of this project is to perform the dynamic modelling and analysis of the compliant joint. This will be done to observe the various dynamic capabilities of the joint.

The project is organized as shown in Fig 1.2 below. In the dynamic analysis, numerical and analytical techniques will be employed on the dynamic model to gain a better understanding of the system. The Harmonic Balance method is the analytical technique that will be used while the fourth order Runge-Kutta will be used to numerically integrate the equation. MSC Adams software will be used to simulate the system and validate the model. The behavior of the dynamic system (chaos, jump phenomenon) will then be observed through the generation of Phase and Frequency response plots

Subsequently, the system dynamics will be investigated to observe the dynamic response when an actuator is added to the joint. A power analysis will as well conducted to obtain the power consumption of the system.

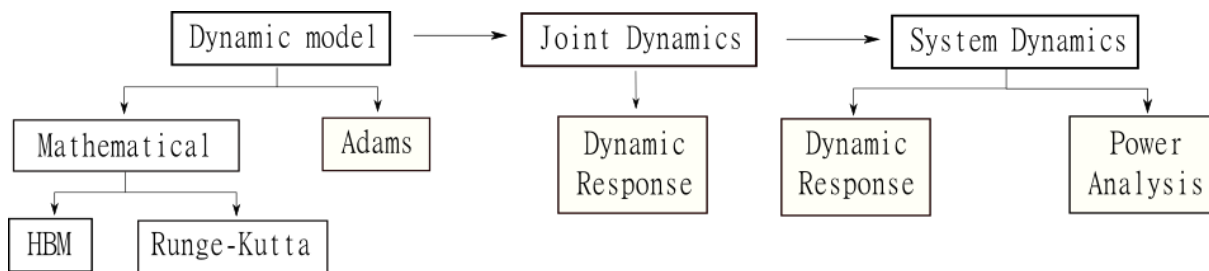


Figure 1.2: Project Outline



## 2 | Nonlinear Dynamic Model

This chapter will consider the dynamic model of the compliant joint, but first the kinematics of the mechanism is summarized below

### 2.1 The compliant joint kinematics

This section is based on [Li and Bai, 2019]. Fig. 2.1 below shows the kinematic principle of the joint.

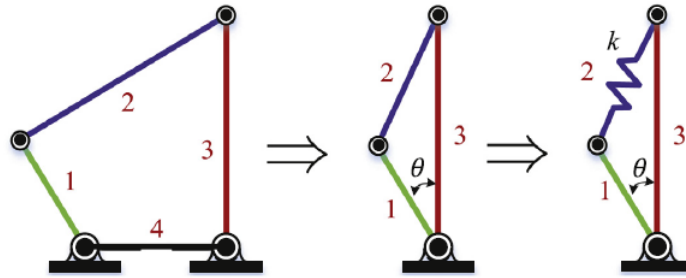


Figure 2.1: The framework of compliant joint using a special case four-bar linkage [Li and Bai, 2019]

In a four-bar rigid-body linkage, the speed ratio between the crank (link 1) and the follower (link 3) is a function of link lengths and rotation angle, so is the torque ratio. In a unique case when the length of link 4 (ground link) is zero, the torque ratio or the reciprocal of the speed ratio becomes 1. When the three links (1-3) are collinear, the linkage becomes singular. If one rigid link is replaced with an elastic element, the stiffness at the singular configuration is zero. The compliant joint mechanism is obtained by replacing the coupler (link 2) with a compliant material (e.g. rubber, spring or thin metal strips) of stiffness  $k$ .

Based on the above mentioned principle, a re-configurable compliant revolute joint mechanism was proposed as shown in Fig 2.2A. The compliant joint is implemented as cable wrapped on three pulleys, one on the output and two on the input link. Two coaxial shafts (input and output), are coupled through the cable. One end of the cable is reeled, while the other end of the cable is connected to a linear spring of stiffness  $k$  with pretension  $F_0$ . The system (joint) is re-configurable by wrapping the cable around different number of pulleys. In this design, the number of pulleys on the input shaft are two times those of the output shaft ( $n$  in Fig 2.2A denotes the number of pulleys on the output shaft). Reconfiguration is also feasible by the cable wrapping pattern as illustrated in Fig 2.2B. Where  $N$  indicates the number of output pulleys wrapped by the cable.

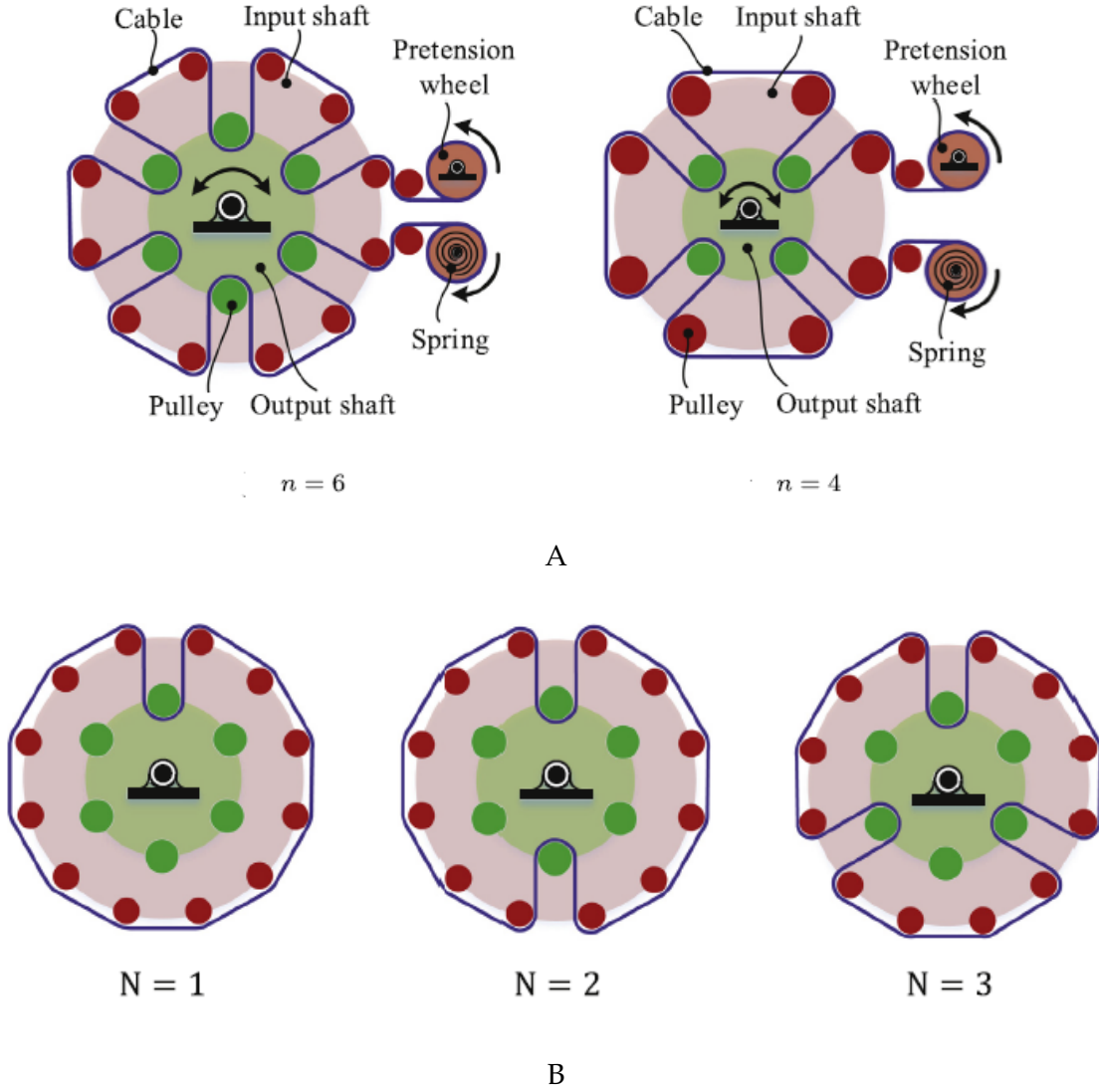


Figure 2.2: (A) Schematic design of joint showing re-configurability through  $n$  (B) re-configurability through  $N$  [Li and Bai, 2019]

The torque generated by the compliant joint is given as

$$T = N^2 k \delta l J_1 + N F_0 J_1 \quad (2.1)$$

where the cable length  $l$  based on the single branch of the compliant joint (shown in Fig. 2.3) is

$$l = \frac{a \cdot \alpha}{2} + |\overrightarrow{DB}| + |\overrightarrow{EG}| \quad (2.2)$$

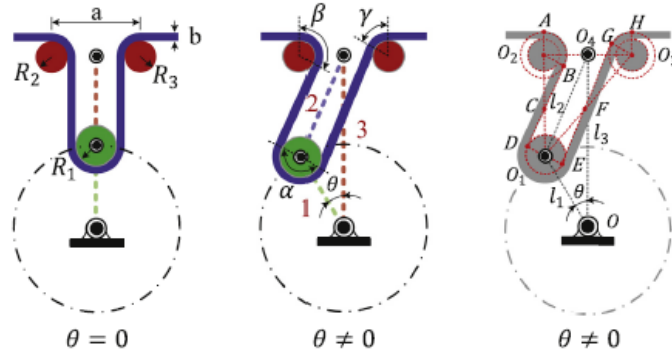


Figure 2.3: Schematic of a single branch of JVSr [Li and Bai, 2019]

$|\vec{DB}| = \sqrt{I_2^2 - al_1 \sin \theta}$ ,  $|\vec{EG}| = \sqrt{I_2^2 + al_1 \sin \theta}$ ,  $\alpha$ ,  $\beta$  and  $\gamma$  are the contact angles between cable and pulley- 1,2,3 respectively, which can also be expressed as

$$\begin{cases} \alpha = \beta + \gamma \\ \beta = \arccos\left(\frac{a - l_1 \sin \theta}{\sqrt{4l_1^2 - 4a_1 \sin \theta + a^2}}\right) - \arccos\left(\frac{a}{\sqrt{4l_2^2 - 4a_1 \sin \theta + a^2}}\right) + \frac{\pi}{2} \\ \gamma = \arccos\left(\frac{a + 2l_1 \sin \theta}{\sqrt{4 + 4a_1 \sin \theta + a^2}}\right) - \arccos\left(\frac{a}{\sqrt{4\frac{1}{4} + 4al_1 \sin \theta + a^2}}\right) + \frac{\pi}{2} \end{cases} \quad (2.3)$$

$J_1$  is the linkage Jacobian ( $J_1 = \frac{\partial l}{\partial \theta}$ ). Given geometric dimensions, the torque becomes a function of cable pretension  $F_0$ , joint configuration  $N$  and  $\theta$  ( $\tau(\theta_p, N, F_0)$ ).

The results of simulation and experiments done in the referenced material showed that the system is able to change its stiffness from zero to a specified range (through design parameters and configurations  $N$ ). The stiffness was also varied in different modes (linear, softening and hardening) by adjusting spring pretension.

## 2.2 Dynamics

Dynamics is the study of systems that undergo changes in their state as time evolves. In mechanical systems such as exoskeletons, the change of states involve motion and the derivation of the equations of motion for the system is the major step in it's dynamic analysis. The equations are fundamental in the design, analysis, and control of the system. They also describe dynamic behavior and they can be used to simulate exoskeleton's motion, design suitable control equations, and evaluate the dynamic performance of the design [Jazar, 2007].

The problems in dynamics may be considered as *Forward* (direct) and *Inverse* [Norton, 2012]. Forward dynamic problems involve the calculation of movements (velocities or accelerations) and external reaction forces, based on known internal forces or moments of force. While, inverse dynamic problems involve the calculation of internal forces or moments of force based on known movements and external forces.

## 2.3 Methods

There are various methods of generating dynamic equations. They all generate equivalent sets of equations, but the method of choice depends on the intended analysis or computation. The Lagrangian formulation will be utilized in this project. It relies on the energy properties of the system to compute the equations of motion. The resulting equations can be computed in closed form, thus allowing the detailed analysis of the system's properties.

### 2.3.1 The Lagrangian method

The Lagrangian equations are a classic formulation of the dynamics of a mechanical system. They reduce the number of equations required to describe the motion of the system from  $n$  (the number of particles in the system) to  $m$  (the number of generalized coordinates) [Murray et al., 1994]. To write the equations of motion, the Lagrangian,  $L$ , is defined as the difference between the kinetic and potential energy of the system:

$$L(q, \dot{q}) = T(q, \dot{q}) - V(q) \quad (2.4)$$

where  $T$  is the kinetic energy and  $V$  is the potential energy of the system, written in generalized coordinates. The equations of motion for a mechanical system with generalized coordinates  $q \in \mathbb{R}^m$  and Lagrangian  $L$  are given by;

$$\frac{d}{dt} \frac{\partial L}{\partial \dot{q}_i} - \frac{\partial L}{\partial q_i} = Q_i \quad i = 1, \dots, m \quad (2.5)$$

where  $Q_i$  is the external force acting on the  $i$ th generalized coordinate. The equation is often represented in vector form as;

$$\frac{d}{dt} \frac{\partial L}{\partial \dot{q}} - \frac{\partial L}{\partial q} = Q \quad (2.6)$$

where  $\frac{\partial L}{\partial \dot{q}}$ ,  $\frac{\partial L}{\partial q}$ , and  $Q$  are to be formally considered as row vectors, though often written as column vectors for notational convenience.

## 2.4 Joint dynamic model

The exoskeleton elbow joint section is assumed to be a 1 degree of freedom (DOF) pendulum system as shown in Fig. 2.4 below

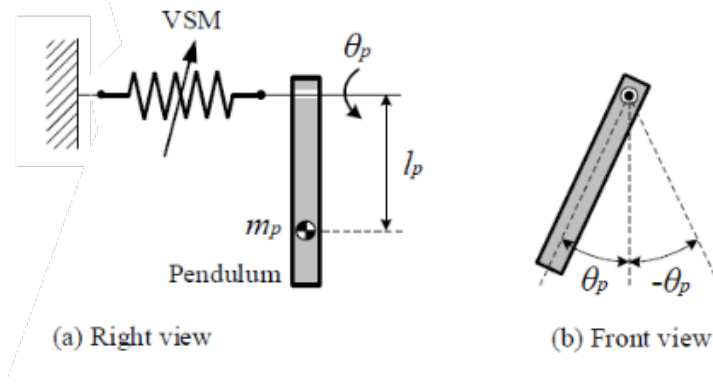


Figure 2.4: Dynamic model of compliant joint, where VSM is Variable stiffness mechanism (The compliant mechanism)

The kinetic and potential energy of the system respectively are

$$T = \frac{1}{2} I \ddot{\alpha}^2 \quad (2.7)$$

$$V = \frac{1}{2} \tau (\theta^2, N, F) - mgl \cos(\theta) \quad (2.8)$$

where  $I$  is moment of inertia,  $\alpha$  is angular acceleration ( $\ddot{\theta}$ ),  $m$  is mass of pendulum, and  $g$  is gravitational acceleration.

Inserting the above equations into Eq. 2.6, if damping is included, gives the dynamic model of the system as

$$I\ddot{\theta}_p + B\dot{\theta}_p + m_p g l_p \sin(\theta_p) + \tau(\theta_p, N, F_0) = 0 \quad (2.9)$$

where  $B$  is angular damping constant  $[N.mm.s/rad]$ . With given values of  $N$  and  $F_0$ , the torque generated by the compliant joint can be simplified to a polynomial that depends only on  $\theta$  such that

$$\tau(\theta) = a\theta \pm y\theta^3 \quad (2.10)$$

where  $a$  and  $y$  are constants depending on the given parameters. This can be done through curve fitting using *least square method* or polynomial interpolation. An example of this using polynomial interpolation (in excel) is shown in Fig. 2.5 below, where  $a = 5,894.9685$  and  $y = 19,584.2465$ . The polynomial fits well with the curve and this is also evident as  $R^2 = 0.9974$

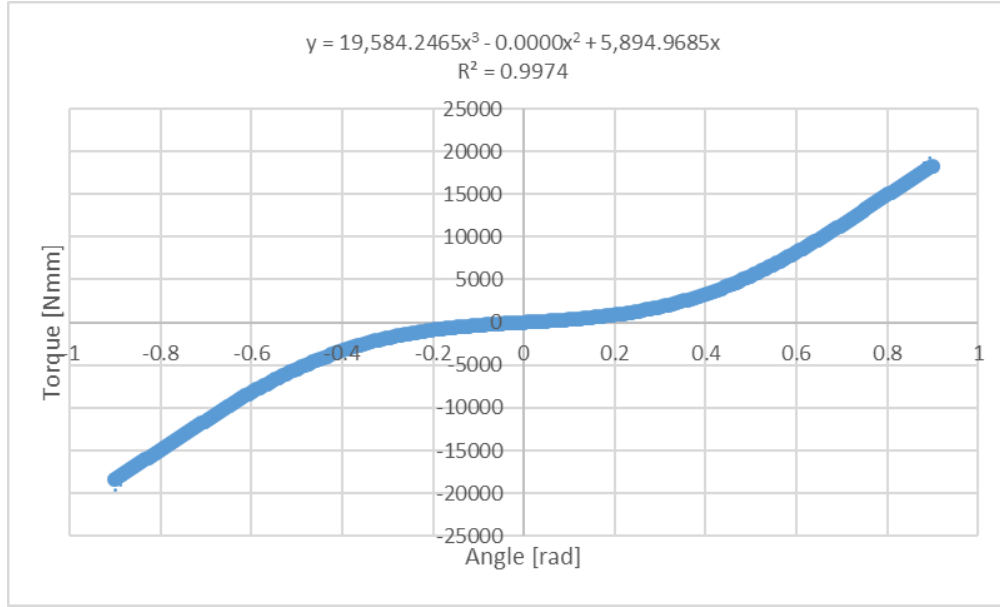


Figure 2.5: Compliant joint torque curve for given geometrical values.  $N = 3$  and  $F_{20}$

Combining this with Eq. 2.9 yields

$$I\ddot{\theta}_p + B\dot{\theta}_p + m_p g l_p \sin(\theta_p) + a\theta \pm y\theta^3 = 0 \quad (2.11)$$

This is similar to the duffing oscillator, which is a second-order nonlinear dynamic equation with static non-linearity, as a result of stiffness [Lumori et al., 2011]. The gravitational torque in Eq. 2.11 above is also a source of non-linearity when the term  $\sin(\theta_p)$  is approximated through Taylor's series expansion as in Eq. 2.12 below. Thus it is essential to note this when considering the nonlinear behavior of the system.

$$\sin(\theta_p) = \theta - \frac{1}{6}\theta^3 \quad (2.12)$$

The next chapter will consider the methods that will be used in solving the dynamic model (Eq. 2.11).

## 3 | Methods

The two methods that will be utilized in solving the dynamic model are the Harmonic balance method (HBM) and Runge-Kutta method. HBM is analytical while Runge-Kutta method is numerical. Both methods including the MSC Adams software that will be used to validate the model are presented. Subsequently, nonlinear dynamic behaviors are discussed.

### 3.1 The harmonic balance method

This is a frequency domain method used to calculate the steady-state response of nonlinear systems. It expresses the periodic response of the system in the form of a Fourier series with finite number of harmonics, whose coefficients are unknowns to be determined. Inserting this response expression into the governing differential equations and balancing the similar harmonic terms, gives a set of nonlinear algebraic equations in terms of the unknown Fourier coefficients [Onur Sert, 2019]. The periodic response in form of Fourier series is given below

$$\begin{aligned}\theta(t) &= \frac{a_0}{2} + a_1 \cos \omega t + a_2 \cos 2\omega t + \dots \\ &\quad + b_1 \sin \omega t + b_2 \sin 2\omega t + \dots \\ &= \frac{a_0}{2} + \sum_{n=1}^{\infty} (a_n \cos n\omega t + b_n \sin n\omega t)\end{aligned}\tag{3.1}$$

where  $\omega = 2\pi/\tau$  is the fundamental frequency,  $\tau$  is the period of oscillation and  $a_0, a_1, a_2, \dots, b_1, b_2, \dots$  are constant coefficients. The physical meaning of the equation is that any periodic function can be represented as a sum of harmonic functions, most periodic functions can be approximated with the help of only few harmonic functions. To demonstrate this method, Eq. 2.11 is simplified to

$$\ddot{\theta} + a\theta + y\theta^3 = 0\tag{3.2}$$

Taking the simplest trial solution of  $\theta \approx A \cos(\omega t)$ , where  $\omega$  represents the nonlinear natural frequency which is amplitude (A) dependent. Substituting the results into Eq. 3.2 gives

$$-\omega^2 A \cos(\omega t) + aX \cos(\omega t) + y(X \cos(\omega t))^3\tag{3.3}$$

Taking the power reduction rule ( $\cos^3(\omega t) = \frac{3}{4}\cos(\omega t) + \frac{1}{4}\cos(3\omega t)$ ) and applying into the equation above, gives

$$(a - \omega^2) A \cos(\omega t) + \frac{y}{4} A^3 [3 \cos(\omega t) + \cos(3\omega t)] \approx 0\tag{3.4}$$

Applying the harmonic balance to the  $\cos(\omega_r t)$  terms (and ignoring the higher harmonics  $\cos(3\omega_r t)$  term) gives the amplitude frequency relationship (Eq. 3.5). Here, the right hand side of the Eq. 3.4 is zero, thus Eq. 3.5 is obtained by merely dividing through with  $\cos(\omega t)$  and subsequently by  $A$ .

$$\omega^2 \approx a + \frac{3y}{4} A^2 \quad (3.5)$$

This relationship (Eq. 3.5 above) is known as the *backbone curve*. It defines the frequency ( $\omega$ ) as a function of the amplitude of response ( $A$ ) of the system when no damping or forcing is present. Fig. 3.1 below shows that the frequency of the response increases with the amplitude  $A$  for the hardening spring (when  $y > 0$ ) and decreases for the softening spring (when  $y < 0$ ). The dotted lines in the figure show the response when the number of terms considered in the harmonic balance is extended to two (the trial solution  $x = A_r (\cos(\omega_r t) + A_{3r} \cos(3\omega_r t))$ , where  $A_{3r}$  is the amplitude of the third harmonic relative to the fundamental amplitude). The figure also illustrated the sufficiency of a one term trial function approximation. The trial solution of the two-term approximation results in Eq. 3.6 below [David Wagg, 2015]

$$\omega_r^2 \approx a + \frac{3y}{4} A_r^2 (1 + A_{3r}) \quad (3.6)$$

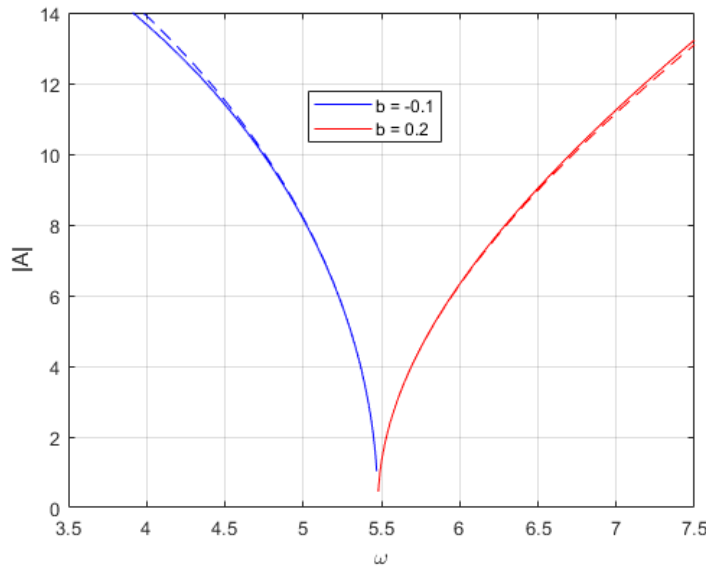


Figure 3.1: Backbone curve showing hardening ( $y > 0$ ) and softening ( $y < 0$ )

When the system is forced, the dynamic model Eq. 2.11 when combined with the approximation  $\sin(\theta) = \theta - \theta^3/6$  becomes



$$\begin{aligned}
I\ddot{\theta} + B\dot{\theta} + m_p g l \left( \theta - \frac{1}{6}\theta^3 \right) + a\theta + y\theta^3 &= T \cos(\omega t) \\
I\ddot{\theta} + B\dot{\theta} + (mgl + a)\theta + \left( y - \frac{1}{6}mgl \right)\theta^3 &= T \cos(\omega t)
\end{aligned} \tag{3.7}$$

Dividing through by the inertia ( $I$ ), gives

$$\ddot{\theta}_p + B_0 \dot{\theta}_p + c\theta + h\theta^3 = T_0 \cos(\omega t) \tag{3.8}$$

where

$$c = (\omega_0 + a/I); h = (y/I - \omega_0/6); B_0 = B/I; T_0 = T/I \quad \omega_0 = mgl/I; \tag{3.9}$$

$T_0$  is considered the amplitude of applied force such that  $T_0 = (A_1^2 + A_2^2)^{1/2}$ ,  $A_1$  and  $A_2$  are constant coefficients as in Eq. 3.1 and the ratio  $A_1/A_2 = \tan^{-1} \phi$ .  $\phi$  signifies a phase shift.

To solve Eq. 3.8 above, the following assumptions are made [Rao, 1995],

- the amplitude  $T_0 = (A_1^2 + A_2^2)^{1/2}$  is considered fixed, but the ratio  $A_1/A_2$  is left to be determined
- $B_0, A_1$ , and  $A_2$  are all small of order  $h$
- the trial solution is a simple harmonic one with a phase shift such that  $\theta = A \sin(\omega t - \phi)$ , the analysis can be simplified by shifting the time origin by  $\tau = t - \phi/\omega$ .

The excitation force becomes  $T_0 \cos(\omega\tau + \phi)$  and the response  $\theta = A \cos(\omega\tau)$ , thus yielding

$$\theta'' + B_0 \theta' + c\theta + h\theta^3 = T_0 \cos(\omega\tau + \phi) \tag{3.10}$$

where  $'$  is derivative with respect to  $\tau$ . Substituting the response  $\theta$ ,  $\theta' = -A\omega \sin(\omega\tau)$  and  $\theta'' = -A\omega^2 \cos(\omega\tau)$  into Eq. 3.10 and using the trigonometric identities, given in Appendix A gives

$$\begin{aligned}
-A\omega^2 \cos(\omega\tau) - B_0 A \omega \sin(\omega\tau) + c \cos(\omega\tau) + hA^3 \left[ \frac{3}{4} \cos(\omega\tau) + \frac{1}{4} \cos(3\omega\tau) \right] \\
\approx A_1 \cos(\omega\tau) - A_2 \sin(\omega\tau)
\end{aligned} \tag{3.11}$$

By disregarding the term  $\cos(3\omega\tau)$  and equating the coefficients of  $\cos(\omega\tau)$  and  $\sin(\omega\tau)$  on both sides of Eq. 3.11 above, it yields the following

$$\begin{aligned} cA - A\omega^2 + \frac{3}{4}hA^3 &\approx A_1 \\ B_0A\omega &\approx A_2 \end{aligned} \quad (3.12)$$

The relationship between the amplitude of the applied force and the quantities  $A$  and  $\omega$  can be obtained by squaring and adding the equations in Eq. 3.12. This gives

$$\left[ cA - A\omega^2 + \frac{3}{4}hA^3 \right]^2 + (B_0A\omega)^2 = T_0 \quad (3.13)$$

### 3.2 Runge-Kutta method

This section is based on [Rao, 1995]. Runge-Kutta is a numerical method that is often used when the motion of the system cannot be integrated in a closed form. It has two fundamental characteristics (as other numerical methods). Firstly, it does not satisfy the governing equation (in this case Eq. 2.9) at all time  $t$  but only at various time intervals  $\Delta t$  apart. Secondly, a fitting variation of displacement  $\theta$ ,  $\dot{\theta}$  and  $\ddot{\theta}$  is assumed within each interval  $\Delta t$ .

This method is stable and self-starting, as the functions values at a single previous point (example  $\theta(t=0)$  and  $\dot{\theta}(t=0)$ ) are needed to obtain the function value at the current point. So for a given value  $\theta_i$  and  $\dot{\theta}_i$ , the approximate formula used for obtaining the next value ( $\theta_{i+1}$ ) from the previous ( $\theta_i$ ) is made to match with the Taylor series expansion of  $\theta$  at  $\theta_{i+1}$  up to terms of order  $(\Delta t)^n$ . The Taylor series expansion for  $\theta(t)$  at  $t + (\Delta t)^n$  is

$$\theta(t + \Delta t) = \theta(t) + \dot{\theta}\Delta t + \ddot{\theta}\frac{(\Delta t)^2}{2!} + \ddot{\ddot{\theta}}\frac{(\Delta t)^3}{3!} + \ddot{\ddot{\ddot{\theta}}}\frac{(\Delta t)^4}{4!} + \dots \quad (3.14)$$

Unlike the Taylor series expansion (Eq. 3.14), which requires higher order derivatives, the Runge-Kutta method does not explicitly require derivatives beyond the first. Second order differential equations are solved by first reducing it to two first order equations. For example, Eq. 2.11 can be rewritten as:

$$\ddot{\theta} = -(B\dot{\theta} + m_p g l \sin(\theta) + a\theta \pm y\theta^3)/I = f(\theta, \dot{\theta}, t) \quad (3.15)$$

Taking  $\theta_1 = \theta$  and  $\theta_2 = \dot{\theta}$ , Eq. 3.15 can be written as two first order equations

$$\begin{aligned} \dot{\theta}_1 &= \theta_2 \\ \dot{\theta}_2 &= f(\theta, \dot{\theta}, t) \end{aligned}$$

by defining

$$\vec{X}(t) = \begin{Bmatrix} \theta_1(t) \\ \theta_2(t) \end{Bmatrix} \text{ and } \vec{F}(t) = \begin{Bmatrix} \theta_2 \\ f(\theta, \dot{\theta}, t) \end{Bmatrix}$$

To find the values of  $\vec{X}(t)$  at different grid points  $t_i$  according to the fourth-order Runge-Kutta method, the following recurrence formula is used

$$\vec{X}_{i+1} = \vec{X}_i + \frac{1}{6} [\vec{K}_1 + 2\vec{K}_2 + 2\vec{K}_3 + \vec{K}_4] \quad (3.16)$$

where

$$\begin{aligned} \vec{K}_1 &= h\vec{F}(\vec{X}_i, t_i) \\ \vec{K}_2 &= h\vec{F}(\vec{X}_i + \frac{1}{2}\vec{K}_1, t_i + \frac{1}{2}h) \\ \vec{K}_3 &= h\vec{F}(\vec{X}_i + \frac{1}{2}\vec{K}_2, t_i + \frac{1}{2}h) \\ \vec{K}_4 &= h\vec{F}(\vec{X}_i + \frac{1}{2}\vec{K}_3, t_{i+1}), \end{aligned} \quad (3.17)$$

$h = t_{i+1} - t_i = \Delta t$ . MATLAB built-in routines “ode23()” and “ode45()” implemented the Runge-Kutta method with an adaptive step-size adjustment, that uses a small/large step-size depending on whether  $f(t)$  is rough or smooth [Won Young Yang, 2005]. Fig. 3.2 shows the response of the system for  $m, l, I = 1$ ,  $B = 0.1$ ,  $a = 0.2$ ,  $y = 2$  and initial conditions  $\theta(0) = 1$ ,  $\dot{\theta}(0) = 0$ . As shown, the Runge-Kutta and the implemented algorithm in MatLab (ode45()) match closely. Thus for the rest of the project, ode45() will be used.

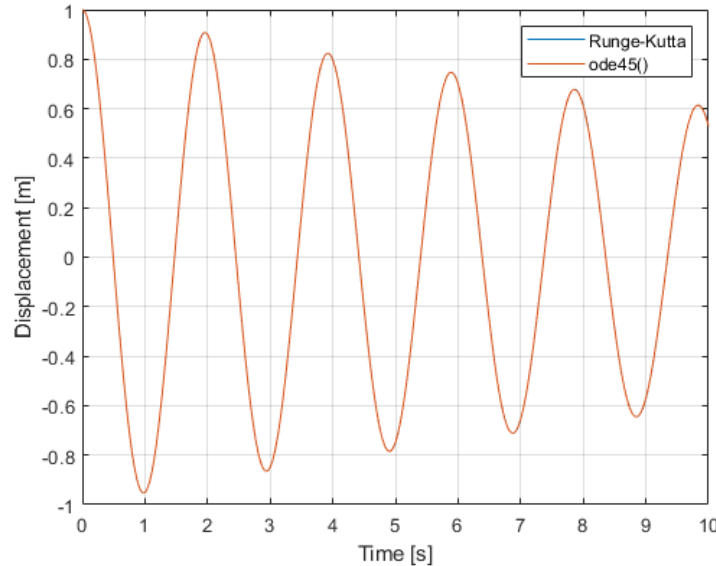


Figure 3.2: Free vibration response for  $\theta(0) = 1$ ,  $\dot{\theta}(0) = 0$  using Runge-Kutta and ode45()

### 3.3 MSC Adams simulation

MSC's software Adams is the most commonly used motion analysis and multibody dynamic simulation software in the world [Adams, 2019]. It helps the user to study the dynamics of moving parts, see the forces and load distribution throughout the system, enhance and optimize the performance of the product. It incorporates real physics by simultaneously solving equations for statics, quasi-statics, kinematics, and dynamics. Adams also runs nonlinear dynamics in a fraction of the time required by Finite Element Analysis (FEA). The theory in this section is based on [Adams/View, 2018].

#### 3.3.1 Integrators

The following are the various integrators available for use in the software.

- GSTIFF (Gear stiff): It is a fast integrator suitable for smooth problems but may have problems at very small time steps
- WSTIFF (Wielenga): Similar to GSTIFF, but adapts better to changes in time step size
- HASTIFF (Hiller-Anantharaman): It is stable at small time steps. It has good accuracy of velocity and acceleration results
- HHT (Hilber-Hughes-Taylor): It is an Integrator from the FEA world, it is stable at small values of the integration step size. For large models the HHT integrator is known to simulate faster
- NEWMARK: Behaves similar to HHT but of a lower order.

#### 3.3.2 Adams Model

The model is set up in Adams as shown in Fig. 3.3. It has the following components; input plate, output plate, 9 pulleys with 9 connecting shafts, a pendulum and a coaxial shaft. There are 6 pulleys and shafts on the input link and 3 on the output link. Both input and output plates are connected to ground via fixed and revolute joints respectively. The coaxial shaft connects the output plate and pendulum through a fixed joint on both ends. The model is based on Computer-aided design (CAD) drawings from the authors Li and Bai [2019].

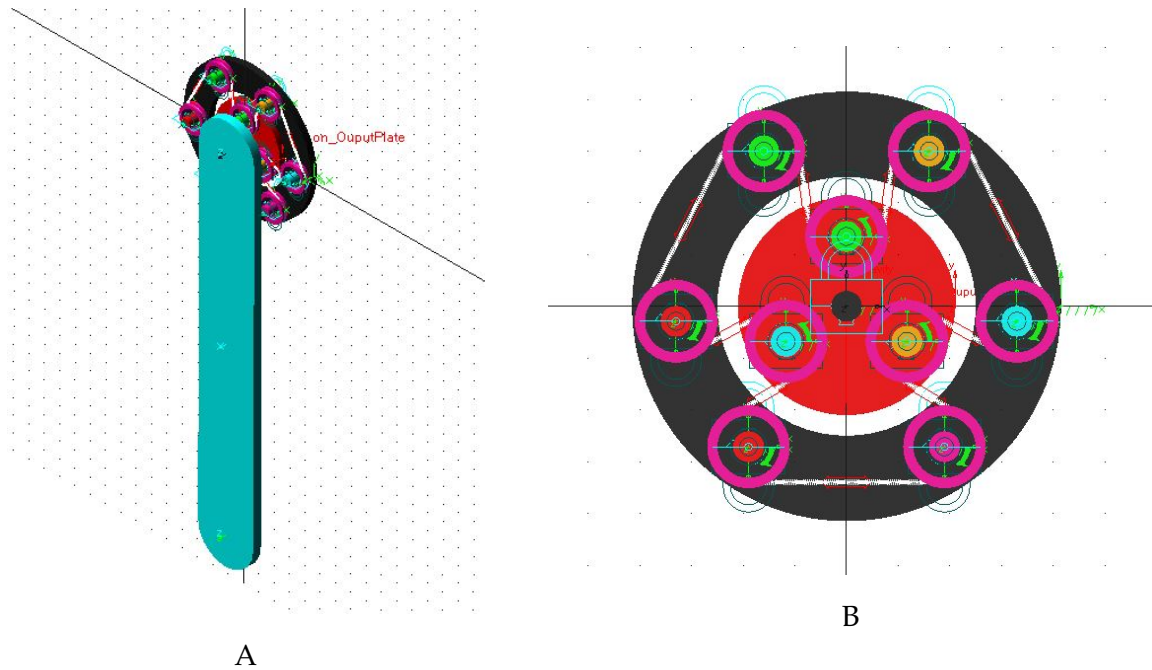


Figure 3.3: (A) Full model (B) Plates, shafts and pulleys

Table 3.1 below shows the mass properties of the model. Where  $I$ ,  $m_p$  and  $l_p$  are moment of inertia (taken at the output coordinate system), mass and center of mass of the pendulum respectively.

Table 3.1: Model Mass properties

Parameter	Values	Units
$I$	748.1990	$kgmm^2$
$m_p$	0.05138	$kg$
$l_p$	93.20	$mm$

The following parameters are options to be included in the definition of the cable.

- Diameter
- Density
- Young's Modulus
- Method - simplified, discretized
- Rkx, Rkb, Rkt - Ratio of longitudinal stiffness, bending stiffness, torsion stiffness respectively.
- Damping ratio
- Velocity - defines initial cable velocity
- Preload - initial cable preload

The cable gets its stiffness (stiffness matrix) definition derived from its cross-sectional dimensions and Young's modulus. The derivation is based on Euler-Bernoulli beam formulation (Eq. 3.18 and Fig. 3.4).

$$\begin{array}{cccccc}
K_{11} & \text{---} & \text{---} & \text{---} & \text{---} & \text{---} \\
\text{---} & K_{22} & \text{---} & \text{---} & \text{---} & K_{26} \\
\text{---} & \text{---} & K_{33} & \text{---} & K_{35} & \text{---} \\
\text{---} & \text{---} & \text{---} & K_{44} & \text{---} & \text{---} \\
\text{---} & \text{---} & K_{53} & \text{---} & K_{55} & \text{---} \\
\text{---} & K_{62} & \text{---} & \text{---} & \text{---} & K_{66}
\end{array} \quad (3.18)$$

For the two methods available, the simplified method gives a fast solution that generates accurate loads on the pulleys, when considering cable mass and neglecting inertia effects with respect to transmission effect. Whereas the discretized cable computes accurate cable vibrations and forces on pulleys, in analysis where the mass and inertia effects of the cable are important. The discretized model allows the definition of all three stiffness ratios (Rkx, Rkb, Rkt), while simplified accepts only Rkx. The ratios are specified as shown in Fig. 3.4 below.

$$\begin{aligned}
K_{11} &= (EA/L) * R_{kx} \\
K_{22} &= (12 E I_{zz}/[L^3 (1+P_y)]) * R_{kx} \\
K_{26} &= (-6 E I_{zz}/[L^2 (1+P_y)]) * R_{kx} \\
K_{33} &= (12 E I_{yy}/[L^3 (1+P_z)]) * R_{kb} \\
K_{35} &= (6 E I_{yy}/[L^2 (1+P_z)]) * R_{kb} \\
K_{44} &= (G I_{xx}/L) * R_{kt} \\
K_{55} &= ((4+P_z) E I_{yy}/[L (1+P_z)]) * R_{kb} \\
K_{66} &= ((4+P_y) E I_{zz}/[L (1+P_y)]) * R_{kb}
\end{aligned}$$

Figure 3.4: Stiffness Ratio

The damping ratio is applied as a multiplier to the stiffness, to obtain the damping coefficient as shown in Fig. 3.5.

#### General Theory

##### Linear Timoshenko theory

$$\begin{aligned}
FX\_Linear &= -K_{11} * (DX-Lo) & -damping\_ratio*K_{11} * VX \\
TX\_Linear &= -K_{44} * AX & -damping\_ratio*K_{44} * WX \\
FY\_Linear &= -K_{22} * DY - K_{26} * AZ & -damping\_ratio*K_{22} * VY - damping\_ratio*K_{26} * WZ \\
FZ\_Linear &= -K_{33} * DZ - K_{35} * AY & -damping\_ratio*K_{33} * VZ - damping\_ratio*K_{35} * WY \\
TY\_Linear &= -K_{35} * DZ - K_{55} * AY & -damping\_ratio*K_{35} * VZ - damping\_ratio*K_{55} * WY \\
TZ\_Linear &= -K_{26} * DY - K_{66} * AZ & -damping\_ratio*K_{26} * VY - damping\_ratio*K_{66} * WZ
\end{aligned}$$

##### Non-linear Euler-Bernoulli formulation

$$\begin{aligned}
FY &= FY\_Linear - FX\_Linear * (6/5/Lo * DY - 1/10 * AZ) \\
FZ &= FZ\_Linear - FX\_Linear * (6/5/Lo * DZ - 1/10 * AY) \\
TY &= TY\_Linear - FX\_Linear * (-1/10 * DZ + 2*Lo/15 * AY) \\
TZ &= TZ\_Linear - FX\_Linear * (-1/10 * DY + 2*Lo/15 * AZ)
\end{aligned}$$

#### General Force in Discretized Cable:

$$\begin{aligned}
FX &= -K_{11} * (DX-Lo) & -damping\_ratio*K_{11} * VX \\
FY &= FY\_Linear - FX\_Linear * (6/5/Lo * DY - 1/10 * AZ) \\
FZ &= FZ\_Linear - FX\_Linear * (6/5/Lo * DZ - 1/10 * AY) \\
TX &= -K_{44} * AX & -damping\_ratio*K_{44} * WX \\
TY &= TY\_Linear - FX\_Linear * (-1/10 * DZ + 2*Lo/15 * AY) \\
TZ &= TZ\_Linear - FX\_Linear * (-1/10 * DY + 2*Lo/15 * AZ)
\end{aligned}$$

Figure 3.5: Damping applied as multiplier to stiffness

### 3.4 Preliminary results

To verify the model discussed above, the simplified cable method will be used and its properties are defined as shown in Table 3.2 below.

Table 3.2: Cable Parameter Adams

	Value	Unit
Diameter	0.9	mm
Density	8E-06	kg/mm <sup>3</sup>
Elastic modulus	1.93E+05	N/mm <sup>2</sup>
Rkx	1.0	—
Damping Ratio ( $\zeta$ )	0.1	—
Velocity	0	mm/s
Preload	0	N

The parameters of the compliant actuator based on the model is given in Table 3.3. A torque of 500 Nmm was applied on the output plate and a simulation was run with the default integrator (GSTIFF). The results matched with the torque model defined by Eq. 2.1 as shown in Fig. 3.6.

Table 3.3: Parameters of the compliant actuator

n	$\lambda$	$\lambda_1$	$l_3$	N
6	0.45	0.267	30 mm	3

where  $\lambda = l_1/l_3$ ,  $\lambda_1 = R/l_3$  and the cable stiffness is defined as

$$k = \frac{EA}{l} \quad (3.19)$$

E, A and l are the Elastic modulus, area and length of the cable respectively. The diameter used is 0.9 mm.

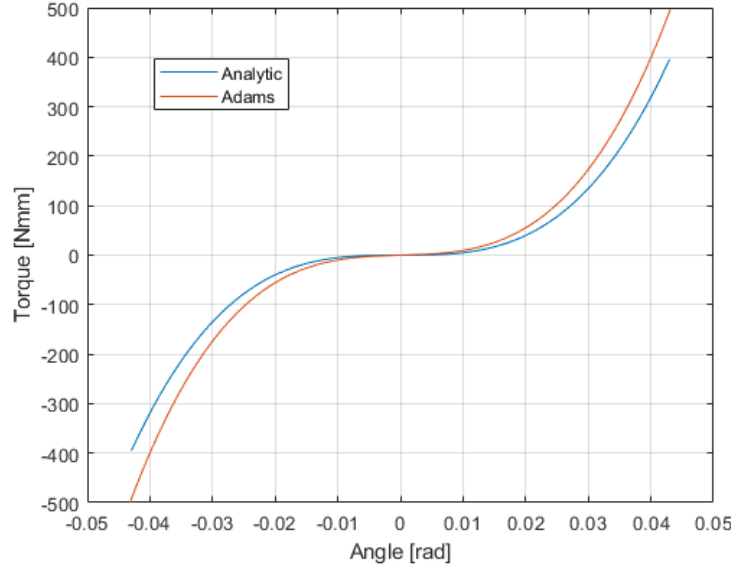


Figure 3.6: Torque versus displacement plot comparison for Adams and analytic

### 3.4.1 Effect of various parameters

To further confirm the Adams model, Fig. 3.7 below shows the effect to the configuration  $N$  and the pretension  $F_0$ , where the full and dash-dot lines denote mathematical and Adams simulation results respectively. Fig. 3.7A shows that as  $N$  increases, hardening behavior is more evident. Fig. 3.7B shows hardening behavior for lower values of  $F_0$ . As  $F_0$  increases, it shifts to softening. While Fig. 3.8 illustrates that as the stiffness increases, the hardening behavior becomes more noticeable. These results are consistent with those obtained by Li and Bai [2019].

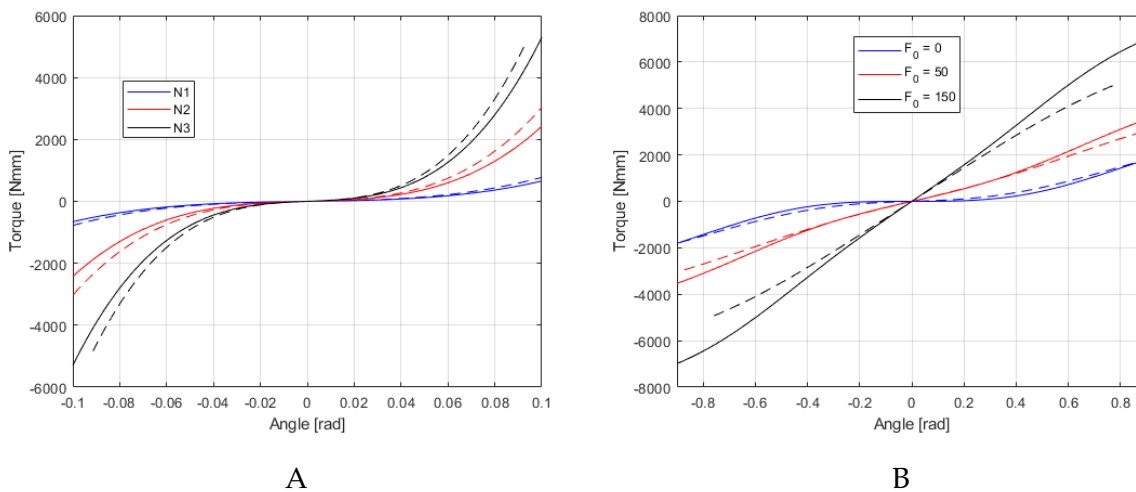


Figure 3.7: (A) Plot of torque versus deflection  $\theta$  based on different configurations for  $F_0 = 20N$ , wherein the full lines denote mathematical results, and the dash-dot lines denote simulation results. (B) different pretension ( $F_0$ ) with  $N = 1$  and  $k \approx 2.8$



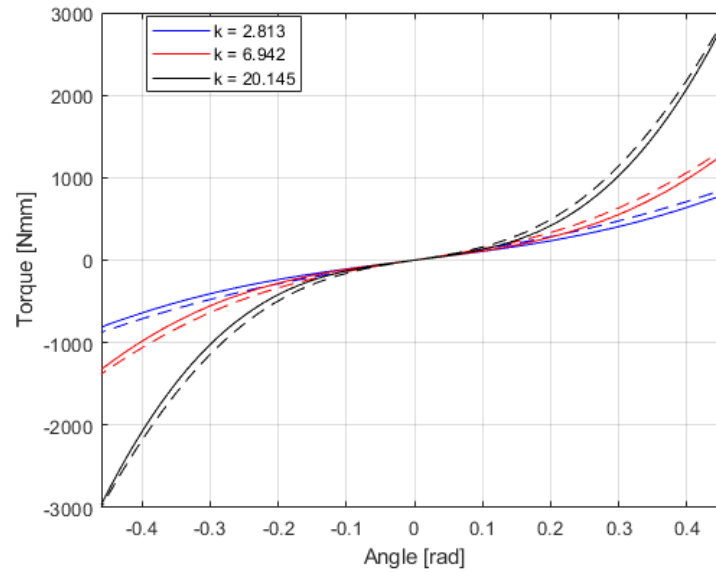


Figure 3.8: (A) Plot of torque versus deflection  $\theta$  based on different stiffness for  $F_0 = 20N$ ,  $N = 1$  wherein the full lines denote mathematical results, and the dash-dot lines denote simulation results

The various stiffness values were obtained in Adams by changing the Young's modulus ( $E$ ) of the cable. The ( $E$ ) values used to obtain the stiffness's shown in Fig. 3.8 are quit unrealistic. This was merely done to validate the Adams model.

## 3.5 Dynamic response

Some of the graphical ways whereby the dynamic response of a system can be observed include displacement-time plot (as shown in Fig. 3.2), phase portrait and frequency response.

### 3.5.1 Phase portrait / Phase plane representation

For a one degree of freedom system, two parameters are needed to completely describe the state of motion. They are usually taken as the displacement and velocity of the system. When used as coordinate axes, the resulting graphical representation of the motion is termed *phase plane representation* [Rao, 1995]. Each point in the phase plane shows a possible state of the system and the state of the system changes with time. A representative point (e.g the state of the system at  $t = 0$ ) in the phase plane moves and traces a curve known as the trajectory and illustrates how the solution of the system varies with time

Fig. 3.9 below shows the phase portrait of Eq. 3.8, (where  $c = 1$ ,  $B = 1$ ,  $h = 0.5$ ,  $T_0 = 0.1$ ,  $\omega = 2.5$ ) solved using Runge-Kutta method with initial conditions  $\theta_0 = 0$  and  $\dot{\theta}_0 = 0$ . The arrows show the trajectory, and the motion of the system follows the path (trajectory). For the rest of the report, the arrows will not be shown in the figures when the phase plane is plotted.

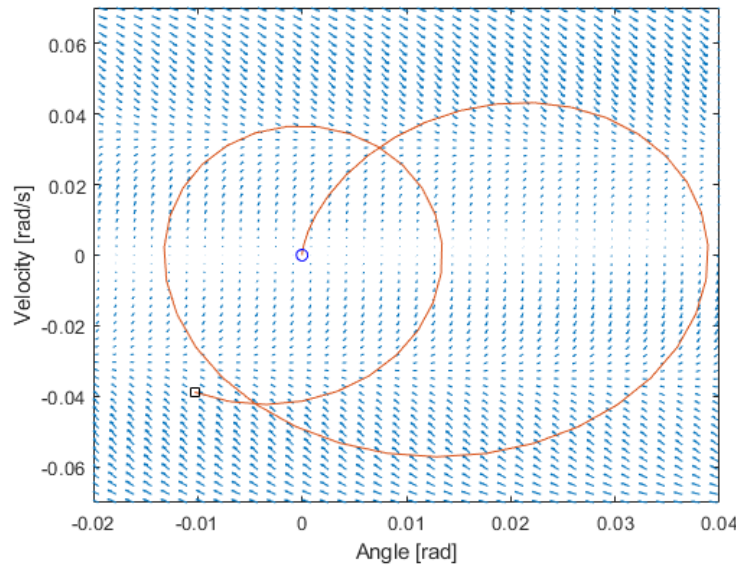


Figure 3.9: Phase portrait

## 3.6 Nonlinear behaviors

### 3.6.1 Chaos

Nonlinear dynamic systems are known to show chaotic behavior for certain parameter values [Kapitaniak, 1990]. Chaos describes the behavior of a system that is naturally unpredictable. That is, it describes the dynamic behavior of a system whose response becomes unpredictable because the non-linearities in the equation greatly amplify the errors in its initial conditions [Rao, 1995].

When viewed as a time series, chaos usually appears to be non-repeatable and non-deterministic, but is in fact very structured [David Wagg, 2015]. It is characterized by being highly sensitive to initial conditions, thus small changes, lead to very quick divergence of behaviour. In this project, the chaotic behavior will be observed from the phase plane representation as in [David Wagg, 2015] and [Rao, 1995]. However the divergence of behavior can be evaluated by computing the rate of separation of initially close starting points as time increases. The *Lyapunov exponents* measures the rate of exponential divergence between nearby trajectories.

### Equilibrium

One type of chaotic behavior that can be observed when considering nonlinear systems is the concept of equilibrium. A linear system has one equilibrium point while a nonlinear system may have multiple equilibrium solutions. This is essential as each equilibrium point may have a different stability property [Inman, 2006]. Stability has however not been considered in this

project.

To illustrate this concept, consider Eq. 3.2 with values as shown in the equation below

$$\ddot{\theta} + 0.0148 - 0.6\theta + 0.6\theta^3 = 0 \quad (3.20)$$

The equilibrium points are obtained by setting the torque stiffness to zero. That is  $0.6\theta - 0.6\theta^3 = 0$ , and the equilibrium points are  $\theta = 0$ ,  $\theta = 1$  and  $\theta = -1$ . Solving the equation with the Runge-Kutta method for 2 different initial conditions gives the result shown in Fig. 3.10. Where for initial condition  $\theta_0 = 1$ , and  $\dot{\theta}_0 = 0.56$ , the solution spirals around the equilibrium condition  $\theta = 1$  (Fig. 3.10). When  $\dot{\theta}_0$  is increased to 0.57, the solution moved clockwise, crossing the point  $\theta = 0$  and spirals around the equilibrium point  $\theta = -1$ . This shows that if there is uncertainty in the initial conditions of the system, then the final state of the system  $\theta = 1$  or  $\theta = -1$  is unpredictable or uncertain [Rao, 1995].

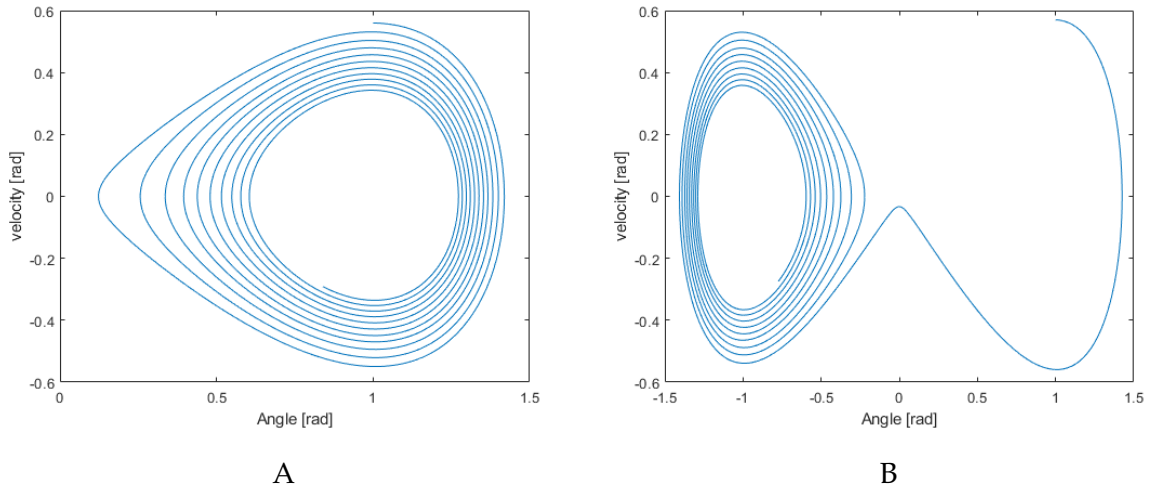


Figure 3.10: Phase-plane trajectories for different initial velocities (A)  $\theta_0 = 1$ ,  $\dot{\theta}_0 = 0.56$  (B)  $\theta_0 = 1$ ,  $\dot{\theta}_0 = 0.57$

### 3.6.2 Jump phenomenon

For nonlinear systems, there exists frequencies at which the vibration suddenly jumps-up or down when it is excited harmonically with slowly changing frequency [Rao, 1995]. The frequencies at which these jumps occur depend upon the non-linearity (hardening or softening) and if the frequency is increasing or decreasing. Between these frequencies, multiple solutions exist and the solution that represents the system depends on the initial conditions Brennan et al. [2008]. An illustration of this is found in Fig. 3.11. For a given constant value of  $T_0$ , the amplitude  $A$  increases from the point 1, 2, 3 as  $\omega$  slowly increases.  $A$  experiences a jump from point 2 to 3. Similarly, as  $\omega$  slowly decreases,  $A$  moves along the points 3, 4, 5, 1. It experiences a jump from point 4 to 5. It is also evident that two amplitudes  $A$  exists for a value of  $\omega$ .

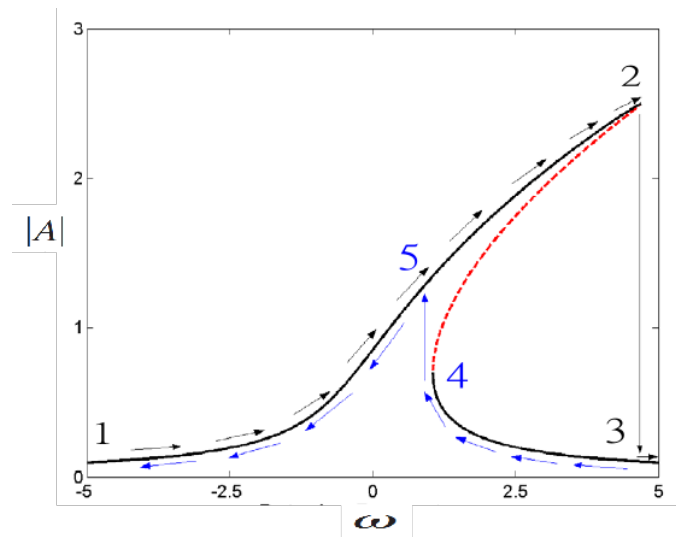


Figure 3.11: Frequency-response curve indicating the jump phenomena [Malatkar et al., 2006]

# 4 | Compliant Joint Dynamics

In this chapter, the dynamics analysis of the compliant joint will be performed (free and forced vibration). Three torque stiffness cases will be considered (linear, hardening, and softening) as shown in Fig. 4.1A for varying pretension  $F_0$ . Where the compliant parameters (for Eq. 2.1) are presented in Table 4.1 and the corresponding parameters for the torque as defined by  $\tau = a\theta + y\theta^3$  is given in Table 4.2. It is important to note that as the simplified polynomial model is used, the results will not fully represent the system. The complete torque plot as described by  $T = N^2k\delta lJ_1 + NF_0J_1$  is shown in Fig. 4.1B

Table 4.1: Parameters of the compliant actuator

n	$\lambda$	$\lambda_1$	$l_3$	N	k
2	0.45	0.267	30 mm	1	2.8 N/mm

The torque curves in Fig. 4.1A show hardening  $F_0 = 20N$ , softening  $F_0 = 150N$  and  $F_0 = 74N$  is meant to show linear behavior and to ensure that the calculation is linear,  $y$  is set to 0 as shown in Table 4.2

Table 4.2: Values of a and y for joint stiffness  $\tau$

	$F_0$ [N]	a	y
$\tau_1$	20	1373.4157	1926.1543
$\tau_2$	74	4283.0136	0
$\tau_3$	150	8378.0031	-510.1081

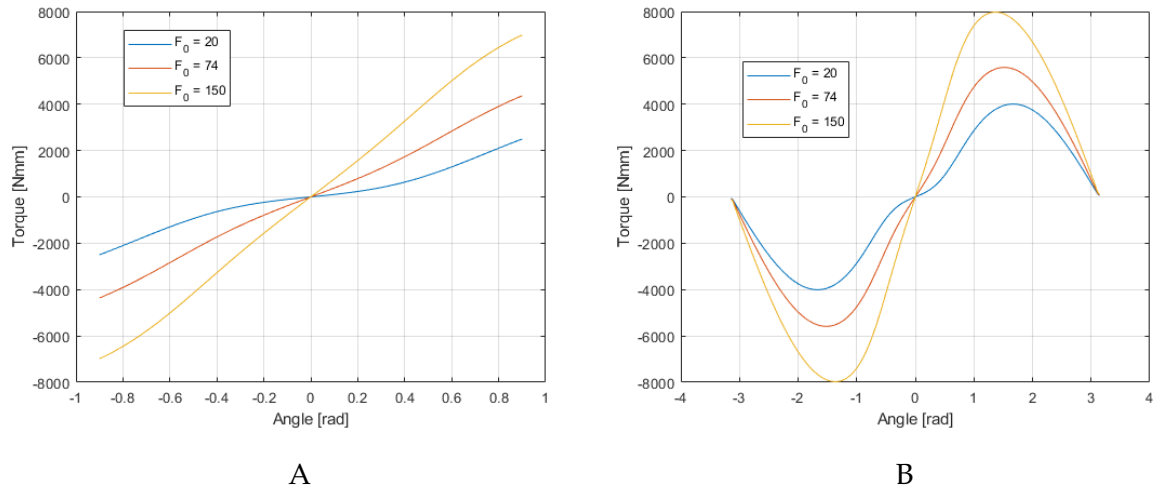


Figure 4.1: Plot of torque versus deflection  $\theta$  for varying pretension ( $F_0$ ) (A) simplified model  $\tau = a\theta + y\theta^3$  (B) Full model  $T = N^2k\delta lJ_1 + NF_0J_1$

To observe the dynamics of the joint as pertaining to the compliant mechanism torque, the

gravitational term in the dynamic equation is ignored and the forced dynamic model (Eq. 3.8), yields

$$\ddot{\theta} + B_0 \dot{\theta} + a_0 \theta + y_0 \theta^3 = T_0 \cos(\omega t) \quad (4.1)$$

where

$$a_0 = (a/I); y_0 = (y/I); B_0 = B/I; T_0 = T/I \quad (4.2)$$

The corresponding model in the frequency domain is given below.

$$\left[ a_0 A - A\omega^2 + \frac{3}{4} y_0 A^3 \right]^2 + (B_0 A \omega)^2 = T_0^2 \quad (4.3)$$

For both equations, the free vibration model is obtained by simply setting  $T_0 = 0$ . The geometric parameters are as given in Table 3.1.

## 4.1 Results and discussion

The results below show the dynamic behavior (phase plane representation and Frequency response) of the compliant joint. Different parameters are varied to show the capabilities of the compliant joint. The values for  $B_0$  and  $T_0$  when not the varied parameter are 0.0295 and 0.6699 respectively

### 4.1.1 Free Vibration - Chaos

The equilibrium point for the linear system  $\tau_2$  is at  $\theta = 0$  and that is shown in Fig. 4.2. As shown, the solution spirals around the equilibrium  $\theta = 0$ . Multiple failed attempts were made to obtain the plots showing the equilibrium points for the nonlinear system (e.g.  $\tau_3$  has equilibrium points at  $\theta = 0, \theta \pm 4.0527$ ). This may be due to equation  $\tau = a\theta + y\theta^3$  not fully capturing the stiffness torque of the system as defined by Eq. 2.1 (see Fig 4.1B). The solution for the equation kept spiraling at the equilibrium point  $\theta = 0$ , similar to the linear system (Fig. 4.2 below)

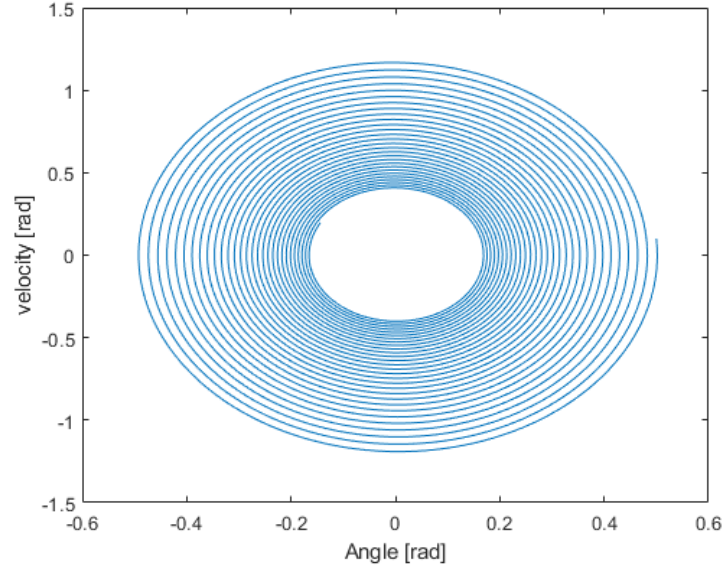


Figure 4.2: Phase plane representation for linear system ( $\tau_2$ ) with initial condition  $\theta_0 = 0.5$   
 $\dot{\theta}_0 = 0.1$

#### 4.1.2 Forced Vibration - Frequency response

##### Varying stiffness

Fig. 4.3 below shows the effects of the three different torque profiles on the frequency response of the system. The non-linearity of  $\tau_1$  and  $\tau_3$  essentially bends the frequency curve, right for hardening ( $\tau_1$ ) and left for softening ( $\tau_3$ ) but stays straight for a linear case. This result is in agreement with [Malatkar et al., 2006]. The response for  $\tau_1$  and  $\tau_3$  is shown clearer in Fig. 4.3B

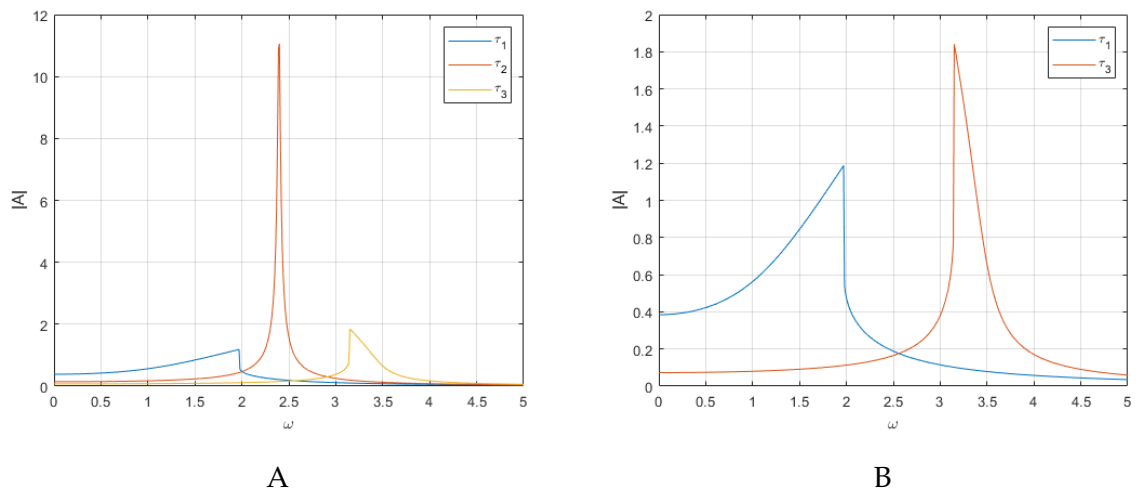


Figure 4.3: Frequency response plot for varying (A)  $\tau_1, \tau_2, \tau_3$  (B)  $\tau_1, \tau_3$

In Fig. 4.4 below, the gravitational inertia is included in the system and as the shown, the

behavior is different from Fig. 4.3. Here the non-linearity of the gravitational inertia is softening as shown Fig. 4.4B where the torque parameters  $a$  and  $y$  are set to 0. This non-linearity, made the behavior of the system including the linear  $\tau_2$  to display a softening behavior as shown in 4.4A for the various torque cases.

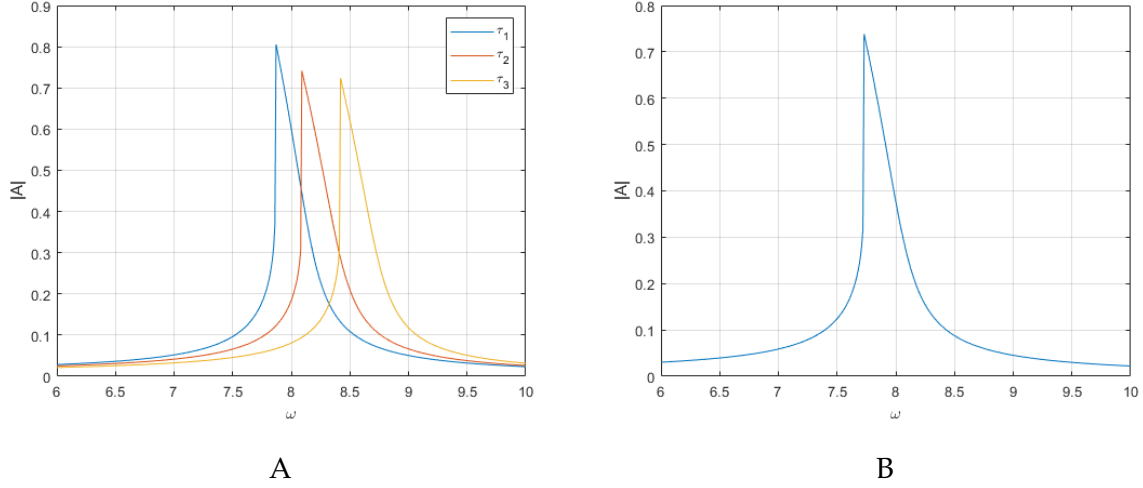


Figure 4.4: (A) Frequency response plot for varying  $\tau_1, \tau_2, \tau_3$  with gravitational inertia (B) Frequency response plot of system when non-linearity is due to only the gravitational inertia term

#### Varying $T_0$ and $B_0$

Fig. 4.5 below shows the response of the system for varying values of forcing amplitude  $T_0$  (Fig. 4.5A) and damping  $B_0$  (Fig. 4.5). An increase in  $T_0$  leads to a increase in the amplitude  $A$  while an increase in  $B_0$  leads to a decrease of  $A$ .

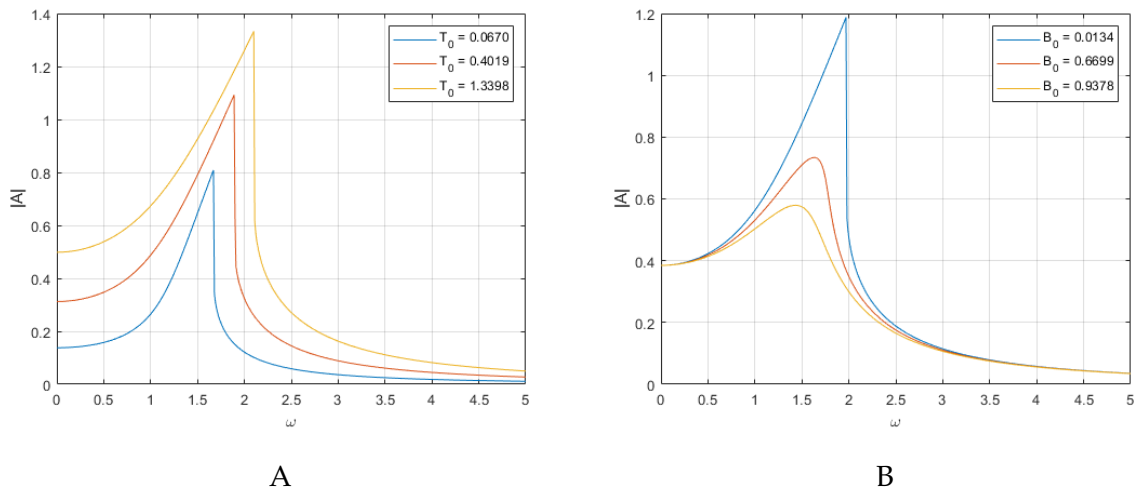


Figure 4.5: Frequency response plot for varying (A)  $T_0$  (B)  $B_0$ , torque profile is  $\tau_1$



### Varying inertia $I$

Fig. 4.6 below shows the effect of inertia  $I$  on the frequency response of the system. As  $I$  increases, the response shifts in frequency  $\omega$  and reduces in amplitude  $A$ .

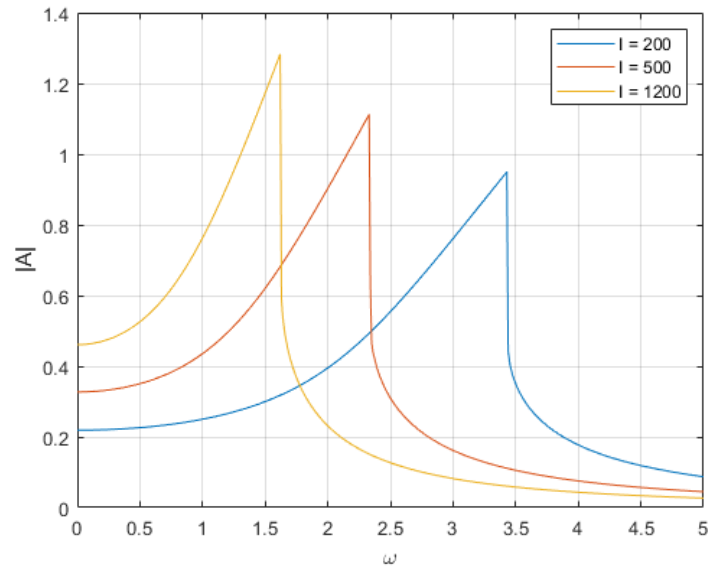


Figure 4.6: Frequency response plot for varying values of  $I$

### Jump phenomenon

The jump phenomenon already exists in the results above but will be illustrated here in Fig. 4.7 for  $\tau_1$  and  $T_0 = 6.6988$ . The amplitude of vibration increases from point 1 to 2 as  $\omega$  slowly increases. It then experiences a jump to point 3 on the curve. It also shows that when  $\omega \approx 2.5$ , two values of amplitudes exists  $A \approx 1.78$  and  $0.8$ , which is in agreement with Section 3.6.2 and [Brennan et al., 2008]. It however, did not capture the second frequency point  $\omega$  and this may be due to how the equation was implemented to obtain the plot or the considered parameter values.

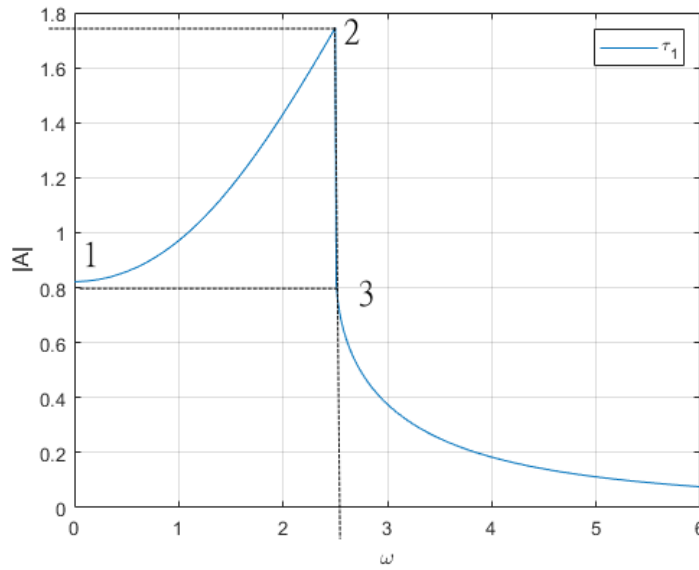


Figure 4.7: Frequency response, illustrating jump phenomenon with torque  $\tau_1$  and  $T_0 = 6.6988$

### 4.1.3 Forced vibration - Phase plane

Small variations in the frequency  $\omega$  or the amplitude of forcing term  $T_0$  can lead to chaos, and this will be illustrated below.  $\tau_1$  is used and when  $T_0$  is varied,  $\omega = 1.5$ , while  $T_0 = 5.5$  when  $\omega$  is varied. The y-axis of the plots presented in this section is in *rad/s*.

#### Varying $T_0$

Fig. 4.8 - Fig. 4.9 show the response of the system (showing both phase plane (A) and time series (B)) for varied values of  $T_0$  with initial conditions  $\theta = 0.8$ ,  $\dot{\theta} = 0$ . When  $T_0 = 6.7$  (Fig. 4.8), a 2 period response is observed (see time series Fig. 4.8B). This changes to an 8 periodic response when  $T_0$  is increased to 6.8 (Fig. 4.10) and becomes chaotic at  $T_0 = 9.0$  (Fig. 4.9). This result is consistent with [Yu et al., 2011]; [K. et al., 2002] and [Rui-Lan et al., 2012].

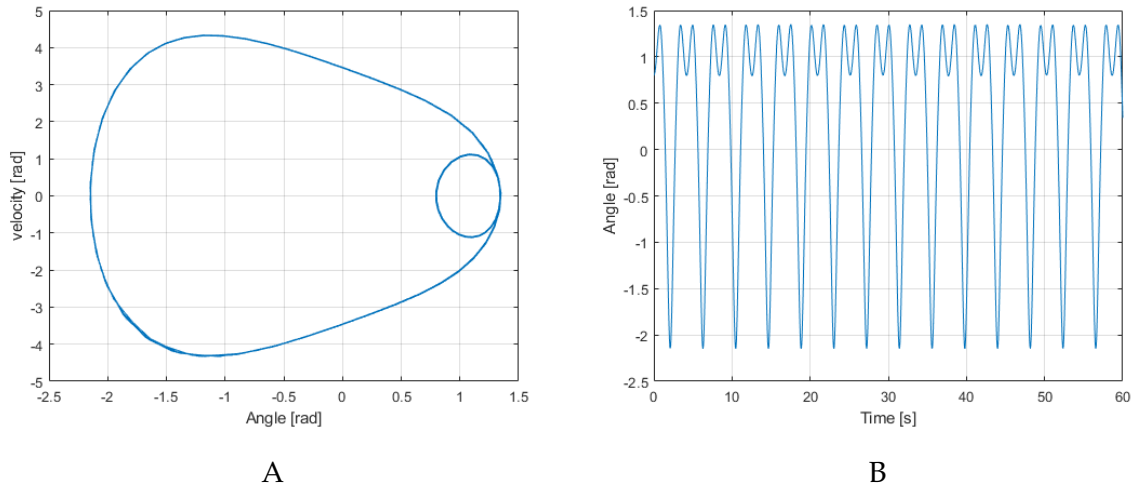


Figure 4.8: (A) Phase plane representation showing 2 period oscillation for  $T_0 = 6.7$  and (B) Time series

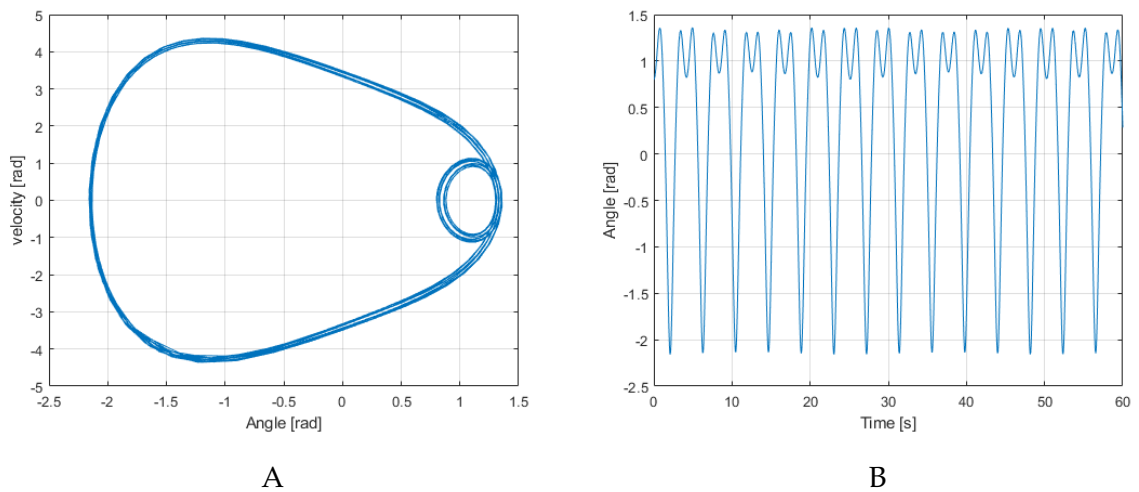


Figure 4.9: (A) Phase plane representation showing 8 period oscillation for  $T_0 = 6.8$  and (B) Time series

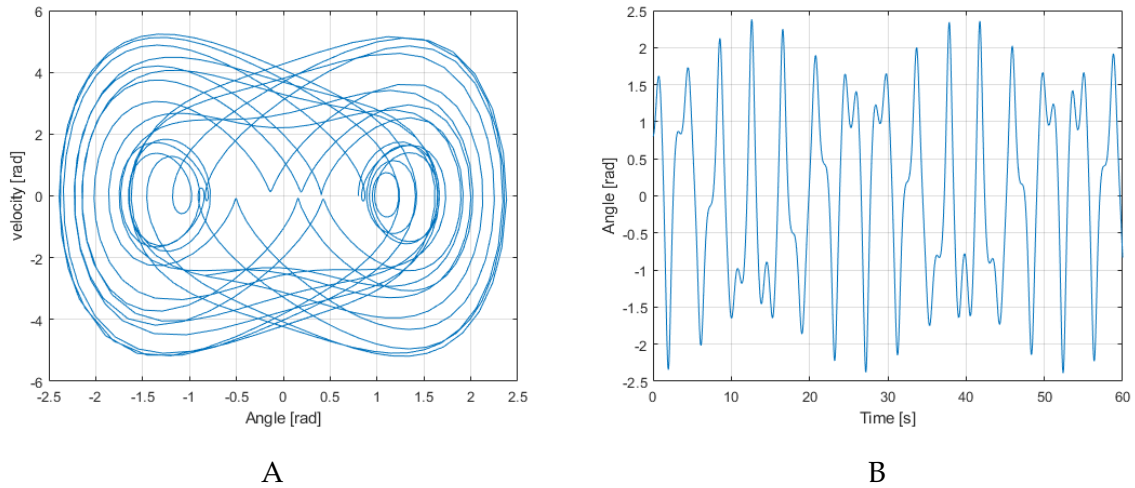


Figure 4.10: (A) Phase plane representation showing chaos for  $T_0 = 9.0$  and (B) Time series

### Varying $\omega$

Fig. 4.11 - Fig. 4.12 show the response of the system for varied values of  $\omega$ . When  $\omega = 2.1$  (Fig. 4.11), a 1 periodic response is observed. Chaos occurs when  $\omega$  is reduced to 1.85 as shown in Fig. 4.12. Initial conditions  $\theta = 1.8, \dot{\theta} = 0$ . This result is consistent with [Yu et al., 2011].

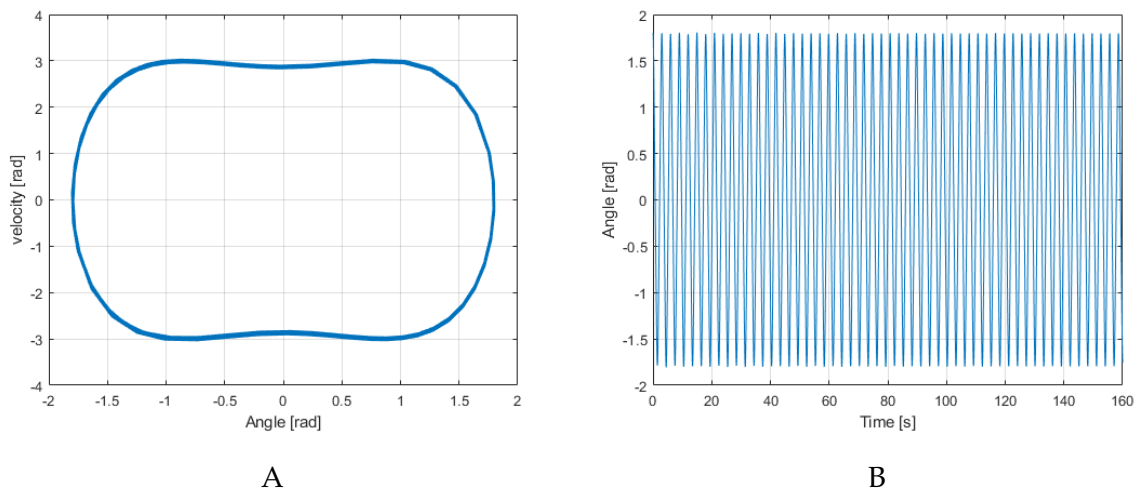


Figure 4.11: (A) Phase plane representation showing one period 1 period oscillation for  $\omega = 2.1$  and (B) Time series

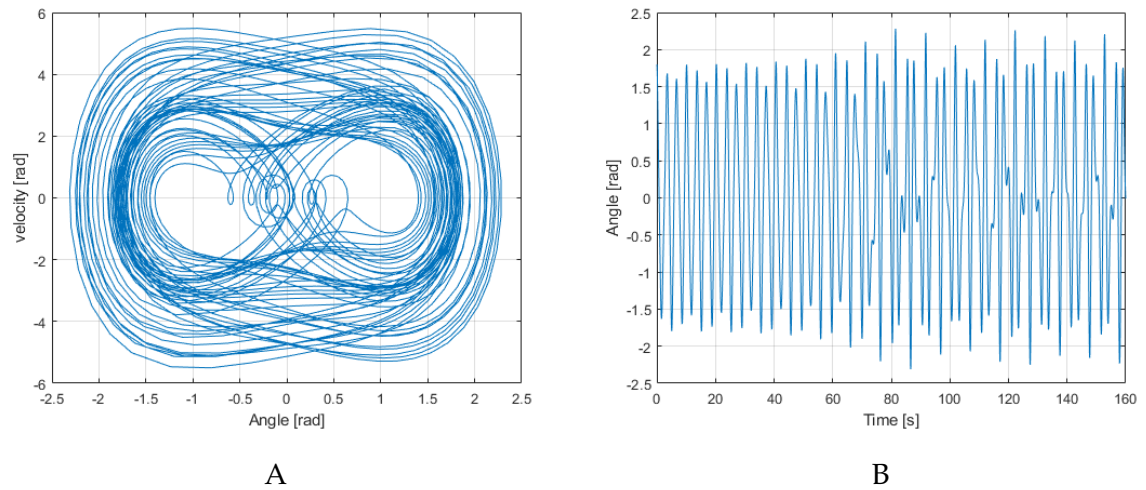


Figure 4.12: (A) Phase plane representation showing chaos for  $\omega = 1.85$  and (B) Time series



# 5 | Model Validation

The dynamic model will be validated by comparing the Runge-Kutta method with Adams simulations. Afterwards, the Runge-Kutta and HBM will be compared. To start of, the damping coefficient will first be determined. This will enable the comparison of Adams and Runge-Kutta.

## 5.1 Determining damping coefficient

A free vibration analysis was done on the Adams model (based on parameters for Fig. 3.6) by giving it an initial displacement of  $0.001 \text{ rad}$ . The results of the analysis was then transfers to MatLab and a nonlinear grey-box model, namely, *idnlgrey* was used to identify the damping ratio (B). The obtained value is  $22 \text{ Nmms/rad}$  and as shown in Fig. 5.1A, it matches with a 94.68% accuracy. The values of  $a$  and  $b$  in Eq. 2.11 is presented in Table 5.1.

Table 5.1: Parameters  $a$  and  $b$  obtained from Adams simulations and analytic calculations

	Adams	Analytic
$a$	6006273.4515	4984676.07666
$y$	375.3128	0.3891

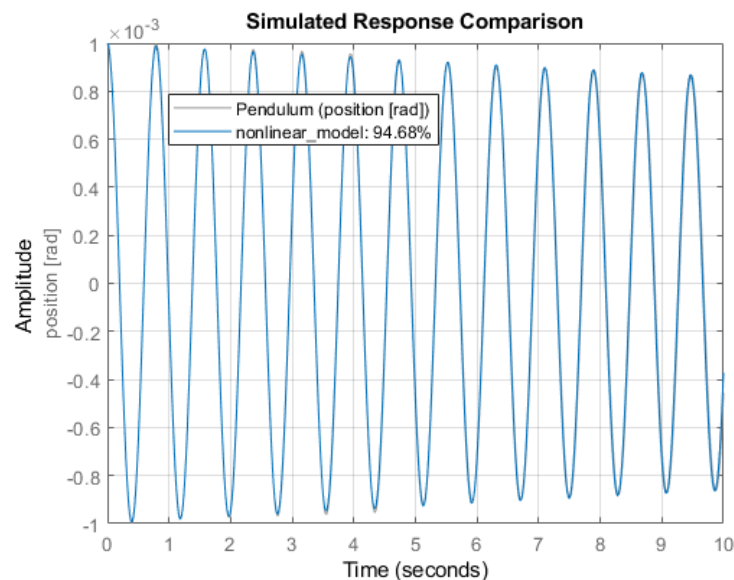


Figure 5.1: non-linear grey-box model

## 5.2 Runge-Kutta vs Adams

### 5.2.1 Free vibration

The value of  $B$  is then inserted into the dynamic model (Eq. 2.9) and solved using the Runge-Kutta method. The result is shown in Fig. 5.2A. The figure shows a good match between the two methods especially between  $t = 0$  to  $t = 5$ , and then begins to slightly deviate. This deviation is shown in the error plot (Fig. 5.2B), starting at 0 up to  $\approx 0.00015$  at  $t = 10$ .

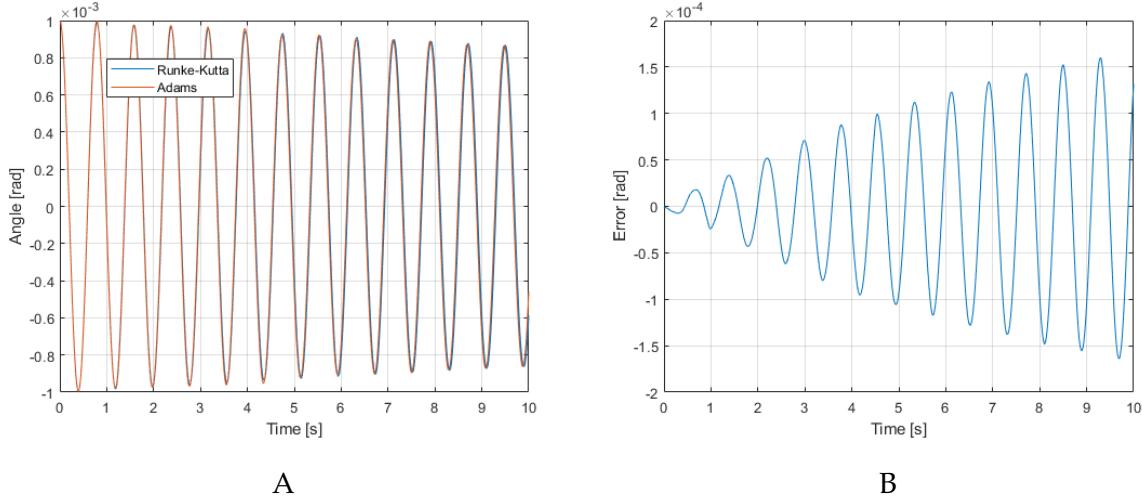


Figure 5.2: (A) Runge-Kutta and Adams free vibration results (B) Error

### 5.2.2 Response under harmonic motion of input plate

For this test, the input plate is given an harmonic motion of  $\theta_b = X \sin(\omega t)$ , where  $X = 3$  and  $\omega = 0.3$ . Neglecting gravitational effects, the dynamic equation becomes

$$I\ddot{\theta}_p - B(\dot{\theta}_p - \dot{\theta}_b) + \tau(\theta_p - \theta_b) = 0 \quad (5.1)$$

where  $\theta_b$  is the angle of the input plate (the base). The torque profile for this simulation is given in Table 5.2 where  $k = 6.942 \text{ N/mm}$ ,  $N = 3$   $F_0 = 0$

Table 5.2: Parameters a and y obtained from analytic calculations

a	y
6600.0619	51342.7229

Solving the equation with initial conditions  $[\dot{\theta}_0 = 0 \ \theta_0 = 0]$  gives the result as shown in Fig. 5.3. Fig. 5.3A shows the output plate oscillating as it follows the trajectory of the input plate but the oscillation later dies out as time is increased (shown in Fig. 5.3B).



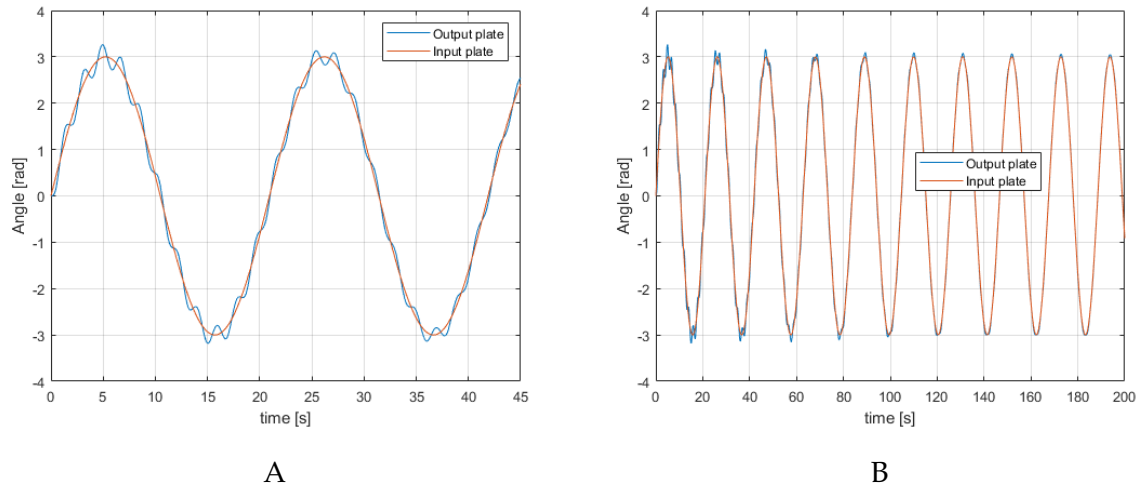


Figure 5.3: Runge-Kutta simulation response of Input and Output plate (A)  $t = 45$  (B)  $t = 200$

In the Adams simulation, gravitational effects are kept on and the results are shown in Fig. 5.4 below. The difference (error) between input and output plate motion is about  $\pm 0.15$  while that of the output plate and pendulum is  $\approx 0$

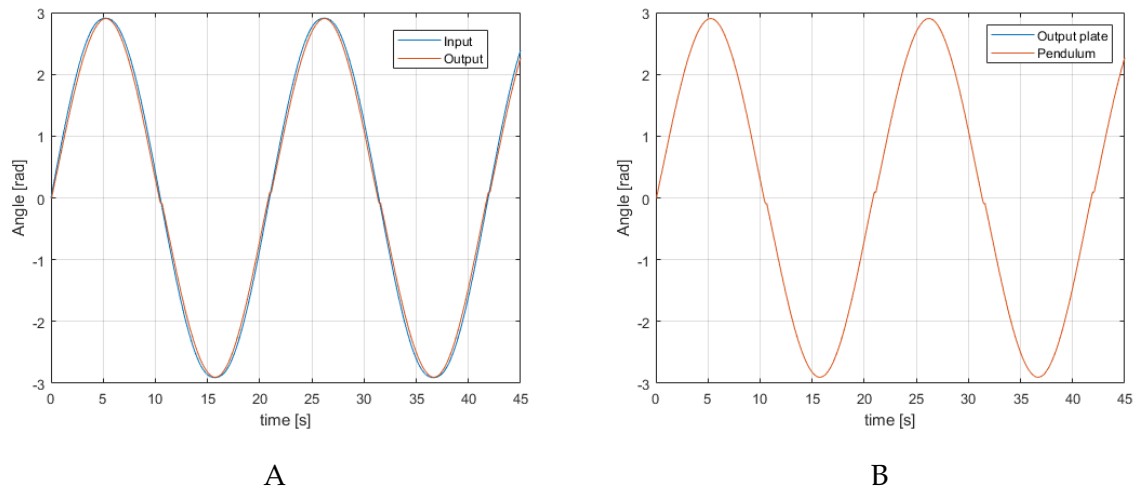


Figure 5.4: Adams simulation response of (A) Input and Output plate (B) Output plate and Pendulum

Fig. 5.5 below shows the comparison between The Runge-Kutta and Adams results for the input plate (Fig. 5.5 A), output plate (Fig. 5.5 B). They closely match and have errors between  $\pm 0.09$  and  $\pm 0.04$  for input and output respectively as shown in Fig. 5.6.

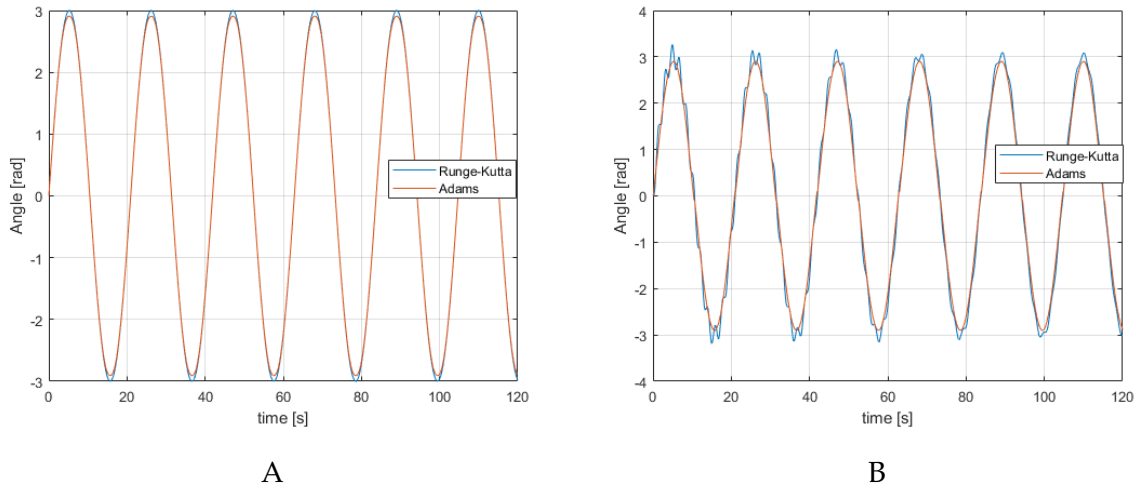


Figure 5.5: Comparison between Runge-Kutta and Adams simulation response of (A) Input plate (B) Output plate

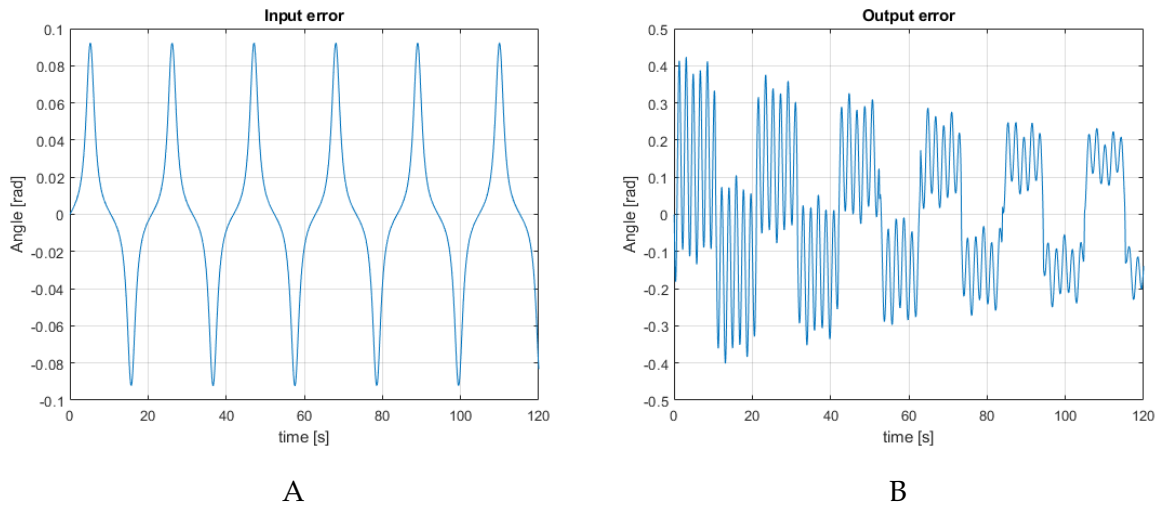


Figure 5.6: (A) Input and (B) Output Error of Runge-Kutta and Adams Method

### 5.3 Harmonic Balance Method Vs. Runge-Kutta

To facilitate the comparison between HBM and Runge-Kutta, the HBM will first be converted from frequency to time domain. Shown in Fig. 5.7 is the frequency domain response of the system where a trial displacement of  $\theta = A\cos(\omega t)$  is used. The stiffness torque profile is as given in Table 5.1 (analytic) while the damping and drive torque are  $22Nmms/rad$  and  $500\cos(\omega t)$  respectively. The inertia, mass and length are as given in Table 3.1

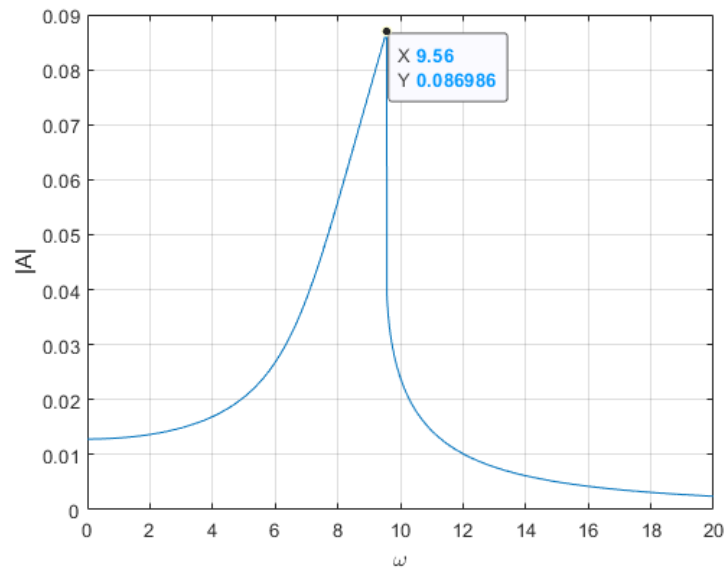


Figure 5.7: Runge-Kutta and Adams free vibration results

From the figure above, the value of the maximum amplitude and corresponding frequency is extracted (that is  $A = 0.08699$  and  $\omega = 9.5600$ ) and used to obtain the angle ( $\theta = A \cos(\omega t)$ ). Fig. 5.8 below shows the comparison between the time response of the two methods as well as the error. The initial conditions for the Runge-Kutta method are  $\dot{\theta}_0 = 0$  and  $\theta_0 = 0.08699$  (max. amplitude  $|A|$ ). The figure shows a good correlation between both methods as the maximum error is at  $\approx 0.008$ .

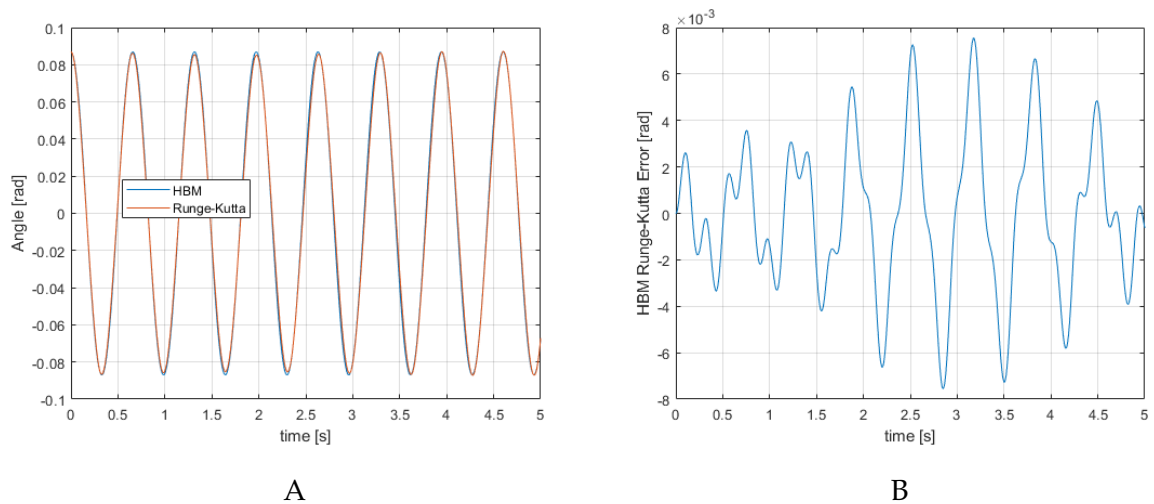


Figure 5.8: (A) Input and (B) Output Error of Runge-Kutta and Adams Method



## 6 | Extended Model Dynamics

The compliant joint will be implemented as an active joint, thus this chapter will extend the model by including an actuator.

### 6.1 Actuators

The purpose of an actuator is to provide torque to a device at a particular joint of interest. This means that the actuator must overcome the weight and resistance of the exoskeleton and allow the user to move easier than without actuation [Ferris et al., 2019].

Several actuator technologies have been used to provide mechanical power to exoskeletons, they include hydraulic, pneumatic, and electric actuators [Gopuraa et al., 2016]. Electric actuators are the most used elements in literature for powered exoskeletons, as they can be controlled with high precision; however, the power-to-weight ratio is not so good [Gopuraa et al., 2016]. Hydraulic and pneumatic actuators have good power-to-weight ratio but do not have much precision.

An electric actuator (motor) is already in use in the upper-limb exoskeleton [Bai et al., 2017]. Thus that will be used in this project and the arrangement of the compliant mechanism and the motor will be considered. Series-elastic actuator and parallel-elastic actuator are presented, to observe the dynamic response and power consumption of both configurations.

The series-elastic actuator (SEA) is a kind of actuator that implements a continuously variable transmission between a motor and a series-elastic element (see Fig 6.1A below). In this case, the series-elastic element is the variable stiffness compliant mechanism. The SEA allows force to be controlled in a simple way [Ham et al., 2009].

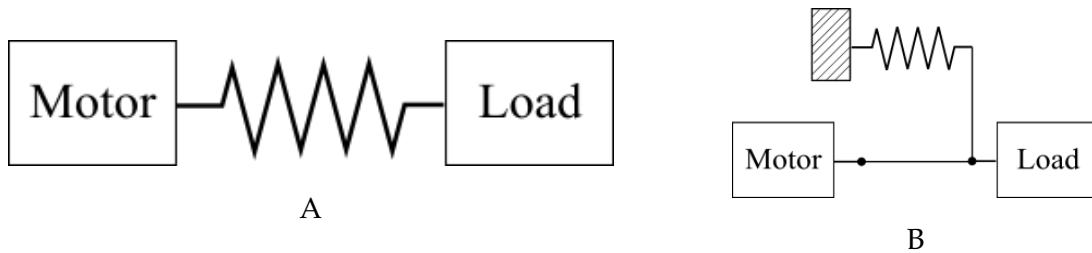


Figure 6.1: (A) Series elastic actuator (B) Parallel elastic actuator

The parallel-elastic actuator (PEA) is shown in Fig. 6.1B. It can also give advantageous power/energy characteristics, if the parallel spring is tuned considering task specific requirements [Beckerle et al., 2016].

## 6.2 Dynamic model

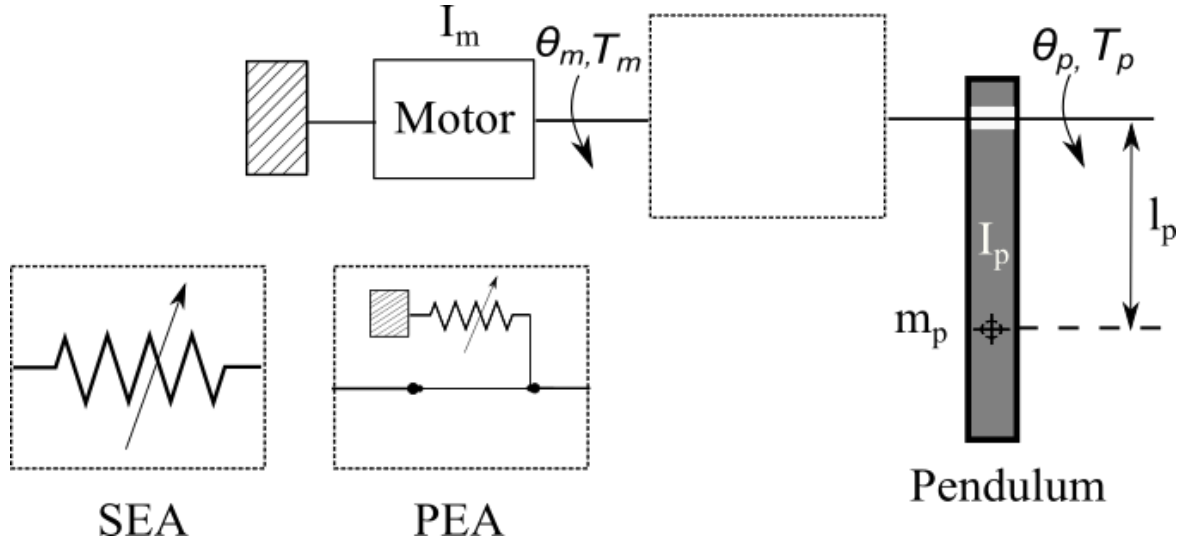


Figure 6.2: Dynamic model including actuators

### 6.2.1 Series Elastic Configuration

From the dynamic model shown in Fig 6.2 above, the equations of motion for series elastic configuration are obtained as in Eq. 6.1 below. The stiffness of the compliant mechanism was reduced from  $\tau(\theta, N, F_0)$  to  $\tau(\theta)$ ,

$$\begin{aligned} I_m \ddot{\theta}_m - \tau(\theta_p - \theta_m) &= T_m \\ I_p \ddot{\theta}_p + m_p g l_p \sin(\theta_p) + \tau(\theta_p - \theta_m) &= 0 \end{aligned} \quad (6.1)$$

where,  $\theta_m$  and  $\theta_p$  represent the motor(input) and pendulum (output) position,  $I_m$  and  $I_p$  are the inertia of the motor and pendulum respectively.  $T_m$  corresponds to the input torque introduced to the joint mechanism by the actuator. Considering that the compliant mechanism already has damping included, the equation becomes

$$\begin{aligned} I_m \ddot{\theta}_m - B(\dot{\theta}_p - \dot{\theta}_m) - \tau(\theta_p - \theta_m) &= T_m \\ I_p \ddot{\theta}_p + m_p g l \sin(\theta_p) + B(\dot{\theta}_p - \dot{\theta}_m) + \tau(\theta_p - \theta_m) &= 0 \end{aligned} \quad (6.2)$$

### 6.2.2 Parallel Elastic Configuration

For the parallel elastic configuration, the dynamic equation of motion is found to be

$$(I_p + I_m) \ddot{\theta}_p + m_p g l \sin(\theta_p) + B(\dot{\theta}_p) + \tau(\theta_p) = T_m \quad (6.3)$$

## 6.3 Dynamic analysis

To investigate the dynamics of the system for SEA, consider Eq. 6.2. Neglecting gravitational effects and multiplying the first equation by  $I_p$  and second by  $I_m$  gives

$$\begin{aligned} I_m I_p \ddot{\theta}_m - B I_p (\dot{\theta}_p - \dot{\theta}_m) - \tau(\theta_p - \theta_m) I_p &= T_m I_p \\ I_p I_m \ddot{\theta}_p + B I_m (\dot{\theta}_p - \dot{\theta}_m) + \tau(\theta_p - \theta_m) I_m &= 0 \end{aligned} \quad (6.4)$$

subtracting the second equation from the first gives

$$I_m I_p (\ddot{\theta}_m - \ddot{\theta}_p) + B(\dot{\theta}_m - \dot{\theta}_p)[I_m + I_p] + \tau(\theta_m - \theta_p)[I_m + I_p] = T_m I_p \quad (6.5)$$

taking the error  $(e) = \theta_m - \theta_p$  and substituting into Eq. 6.5 above, gives

$$I_m I_p \ddot{e} + B \dot{e}[I_m + I_p] + \tau(e)[I_m + I_p] = T_m I_p \quad (6.6)$$

### 6.3.1 Results and discussion

This section show the result of the system dynamic investigation for SEA. In this analysis, the 3 torque cases of linear, hardening and softening as considered in Chapter 4 will be used. For geometric parameters,  $I_p = 746.4011 \text{ kgmm}^2$  (mass of pendulum defined by the Adams model),  $I_m = 0.554 \text{ kgmm}^2$  (taken from the data-sheet of a 22 mm diameter motor shown in Appendix B) and  $B = 22 \text{ Nmms/rad}$ .

Evaluating the Eq. 6.6 for hardening case using the Runge-Kutta method with initial conditions of  $e_0 = 0.01$ ,  $\dot{e}_0 = 0$  gives the time-series response as shown in Fig. 6.3. When the external torque is harmonic,  $e$  shows an harmonic motion with values between  $\pm 2.3$ . While for constant  $T_m$ , it increases at the beginning and remains constant at  $\approx 2.3$  and is zero when  $T_m = 0$

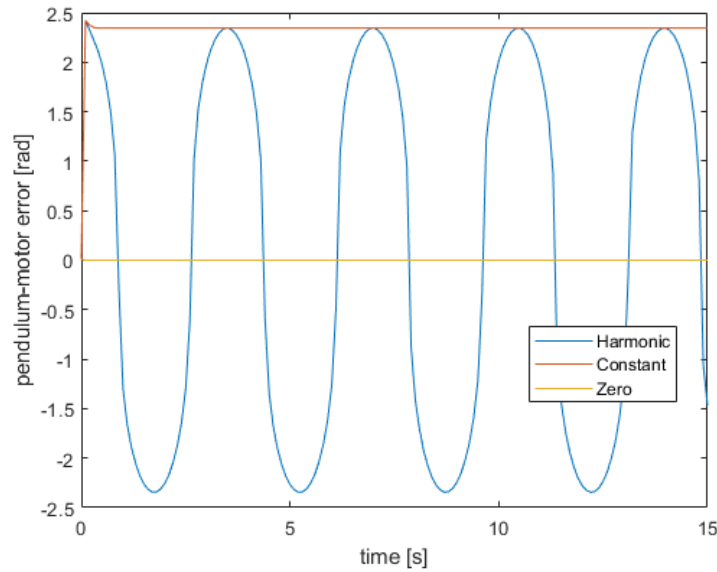


Figure 6.3: Time-series response for various external torque  $[T_m \cos(\omega t) \ T_m \ 0]$  where  $\omega = 1.8$  and  $T_m = 28100$

Fig. 6.4 below shows the frequency response of the system for varying values of  $I_m$  and as shown, although  $I_m$  is small when compared to  $I_p$ , the effect is still evident. As shown in Chapter 4 for  $I_p$ , an increase in  $I_m$  also shifts the response of the system to the right and reduces the amplitude  $A$ .

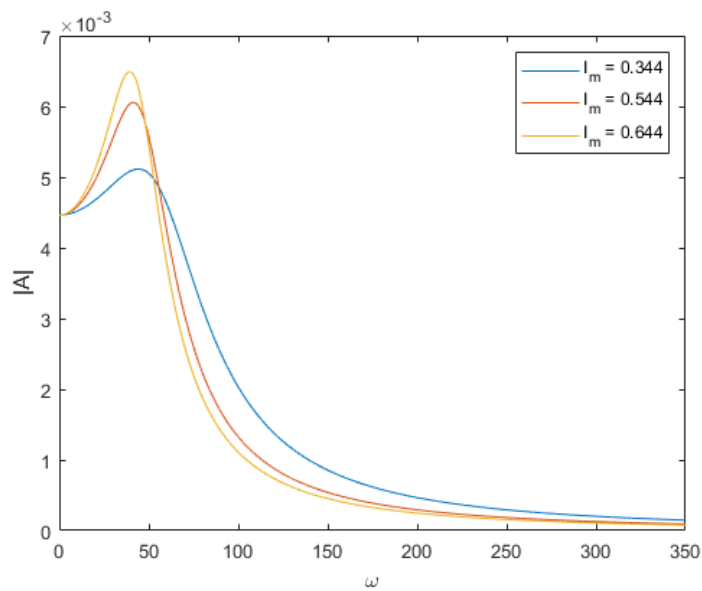


Figure 6.4: Frequency response while varying  $I_m$

Fig. 6.5 below shows the frequency response of the system for varied values of  $\tau$ .  $\tau_3$  which represents softening appears to show a linear behavior as  $\tau_1$ . The system also does not experience the jump phenomenon behavior.



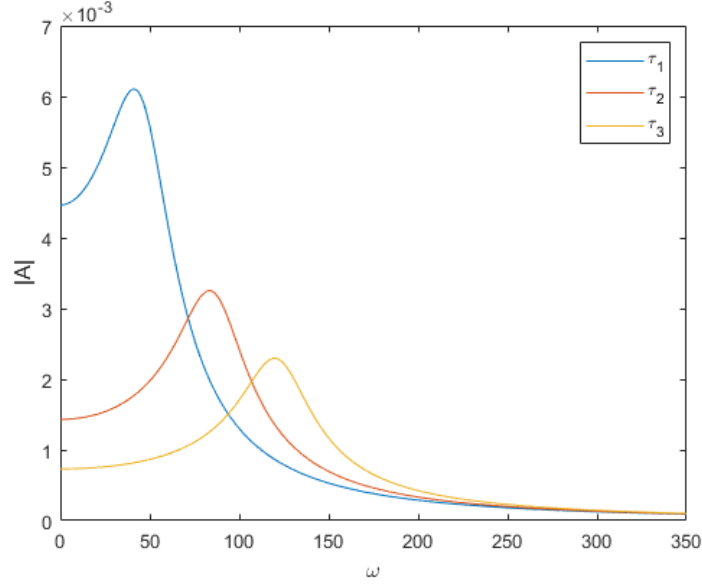


Figure 6.5: Frequency response while varying  $\tau$ , where  $\tau_1$ ,  $\tau_2$  and  $\tau_3$  are hardening, linear and softening respectively

When considering the phase portrait of the system, unlike in chapter 4 where the response went from periodic to chaotic for given values of  $\omega$  or  $T_0$ , the response here retains a certain shape for a wide range of values. An example of this is shown in Fig. 6.6 below where the response revolves around point zero as a spherical shape. The major difference between Fig. 6.6A ( $T_m = 50$ ) and Fig. 6.6B ( $T_m = 1000$ ) is the range of values of  $e$  and  $\dot{e}$ .

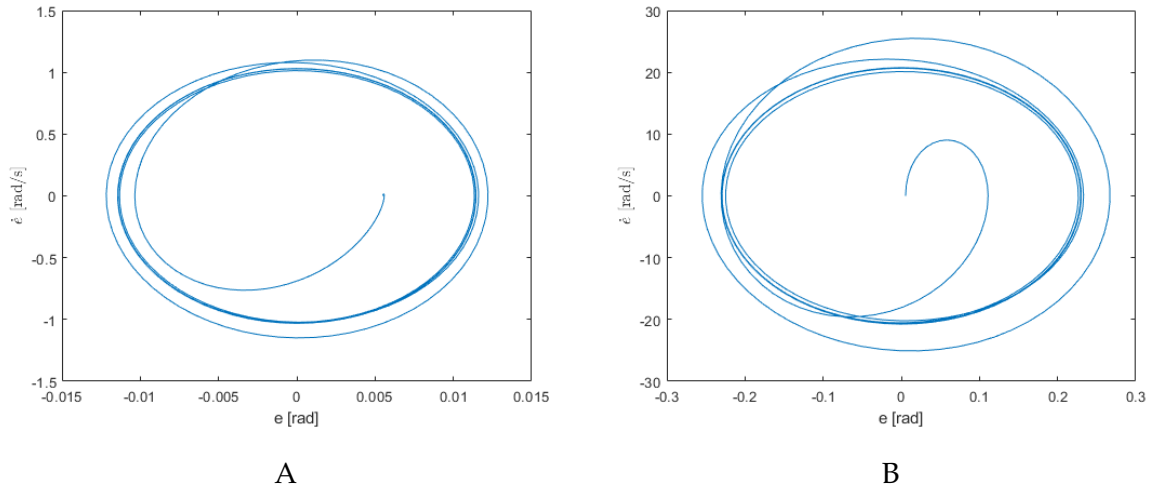


Figure 6.6: Phase plane representation with harmonic force  $T_m \cos(\omega t)$  (A)  $T_m = 50$  (B)  $T_m = 1000$ .  $\omega = 90$ , initial conditions  $e = 0.0055$   $\dot{e}_0 = 0$ ,  $\tau_3$

## 6.4 Power analysis

The power required to perform the motion of input (Eq. 6.7) is investigated based on the models specified for SEA (Eq. 6.2) and PEA (Eq. 6.3).

$$P = T_m \dot{\theta}_m \quad (6.7)$$

The SEA configuration has 2 equations describing the system (Eq. 6.2). To solve this, the displacement of the pendulum  $\theta_p$  is assumed known and used to solve for  $\theta_m$  in Eq. 6.2B. Both  $\theta_p$  and  $\theta_m$  are then used to obtain  $T_m$  in Eq. 6.2A. For PEA configuration, perfect trajectory is assumed such that  $\theta_p = \theta_m$ . Hence, inverse dynamic analysis will be utilized for the simulations that follow.

### 6.4.1 Results and Discussion

To facilitate this analysis, four torque scenarios will be considered as shown in Fig. 6.7 below. The figure shows two hardening ( $F_0 = 20, 150\text{N}$ ) and two softening ( $F_0 = 450, 650\text{N}$ ) behaviors for a compliant joint having parameters as in Table 3.2,  $N = 3$ ,  $k = 2.8 \text{ N/mm}$ . The values corresponding to the definition of the joint stiffness based on  $\tau = a\theta + y\theta^3$  are as shown in Table 6.1 below. The geometric parameters are as defined in Table 3.1, with  $I_m = 0.554$

Table 6.1: Values of  $a$  and  $y$  for joint stiffness  $\tau$

	$F_0$	$a$	$y$
$\tau_1$	20	5,895.9685	19,584.2465
$\tau_2$	150	26,908.7307	12,275.4591
$\tau_3$	450	75,402.0280	-4,590.9733
$\tau_4$	650	107,730.8928	-15,835.2616

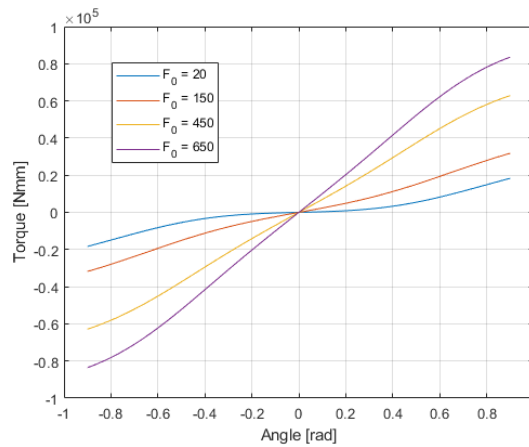


Figure 6.7: Plot of torque versus joint deflection ( $\theta$ ) for varying pretension  $F_0$ .  $N = 3$ ,  $k = 2.3\text{N/mm}$

Fig. 6.8 below shows the time response for the series-elastic configuration obtained by setting  $\theta_p = 0.45\sin(1.8t)$  and solving Eq. 6.2A for  $\theta_m$  using Runge-Kutta method with initial conditions ( $\theta_m$  and  $\dot{\theta}_m = 0$ ). With this, the assumption of perfect trajectory for PEA, can be said to be valid.

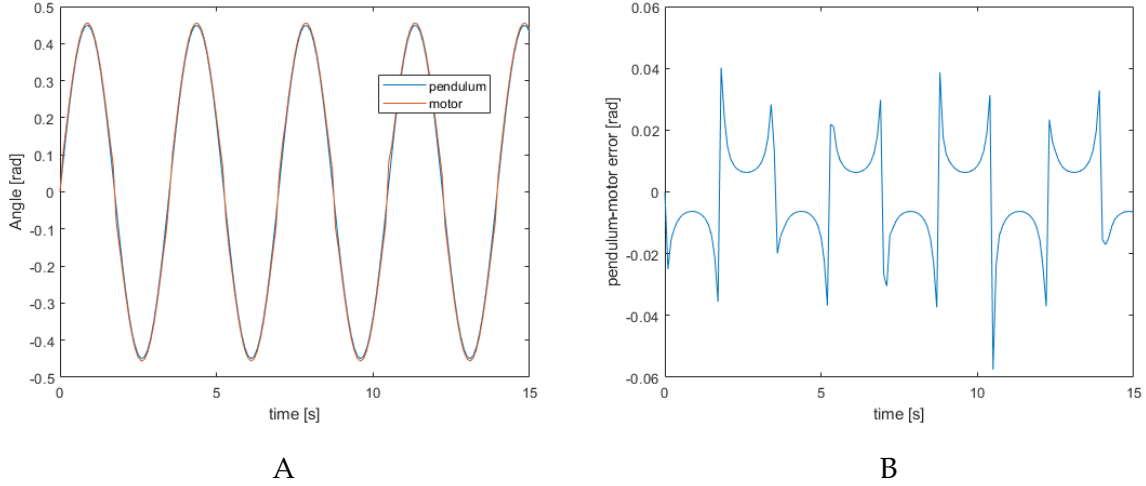


Figure 6.8: (A) SEA dynamic response of pendulum and motor (B) Error between pendulum and motor position

Fig. 6.9 below shows the maximum (peak) power of both SEA (Fig. 6.9A) and PEA (Fig. 6.9B) configurations. In both figures, the peak power increases as stiffness softens. It is common to use springs in exoskeleton joints to assist the motor and reduce the value of the peak power [Grimmer and Seyfarth, 2011]. And with the compliant joint, various the peak power can easily be reduced or increased (by increasing or reducing the pretension  $F_0$ , N or compliant parameters) depending on the power required to complete a desired motion

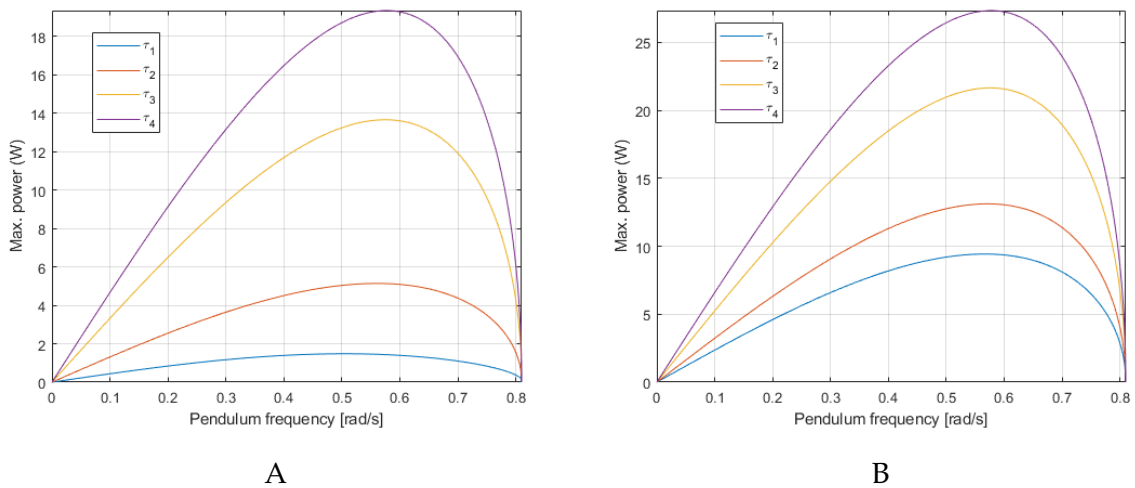


Figure 6.9: (A) SEA max power corresponding to the softening and hardening stiffness behavior (B) PEA max power corresponding to the softening and hardening stiffness behavior of joint stiffness

Fig. 6.10 below shows the comparison between the SEA and PEA peak power for  $\tau_1$ . As shown, the peak power for PEA is much higher than that of SEA configuration.

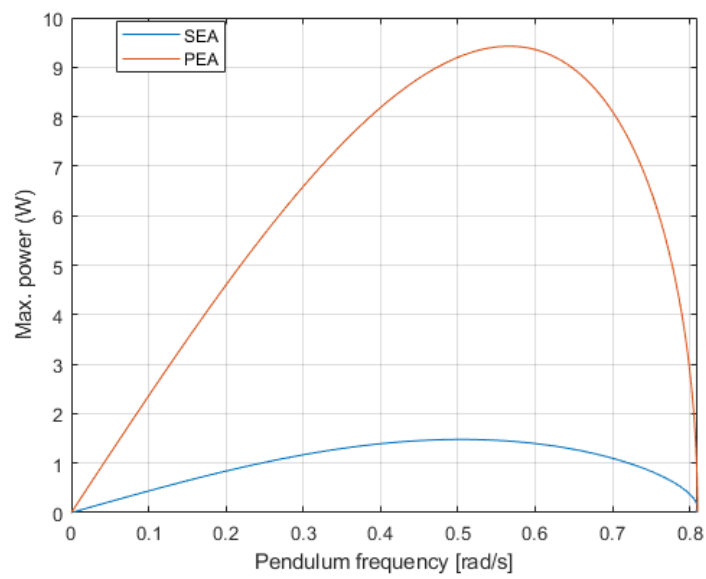


Figure 6.10: SEA and PEA maximum power for  $\tau_1$

## 7 | Conclusion

The objective of this project was to perform the dynamic modelling and analysis of a compliant joint mechanism. It was done to observe the various nonlinear dynamic capabilities of the mechanism. The compliant joint was successfully modelled using the Lagrangian method, numerical Runge-Kutta and analytical Harmonic balance method were utilized in solving the dynamic equation. Both methods were used to show the chaotic and jump phenomenon behaviors associated with nonlinear systems. The behaviors were observed through phase plane representation and frequency response respectively.

This study showed that the non-linearity of the system was not only caused by the compliant joint but also the gravitational term. It also showed that slight changes in system parameters can make the response go from periodic to chaotic. The system, however, did not capture the chaotic nature of equilibrium points and this was associated with the simplification made for the torque generated by the compliant mechanism.

The study also showed that the generated dynamic mode of the compliant joint is valid. This is due to the comparable results between MSC Adams and Runge-Kutta method. The comparison was done for free-vibration and harmonic forcing on the input plate of the compliant joint. The difference in results for the free-vibration ranged between 0 (at  $t = 0$ ) to  $0.00015 \text{ rad}$  (at  $t = 10$ ). While for the harmonic forcing, errors ranged between  $\pm 0.09$  and  $\pm 0.04$  for input and output respectively. Afterward, the harmonic balance method and Runge-Kutta were compared and the results matched closely with an error between  $\pm 0.008$ . It also showed that the one-term approximation used in obtaining the frequency response of the system was sufficient.

The model was further extended to include an actuator. Series elastic (SEA) and Parallel elastic (PEA) actuators were considered. The dynamics of the system for SEA was observed and did not capture chaos and jump phenomenon. The results also showed that when  $\omega$  is varied, the phase plane representation retained a similar shape and the difference was in the values of the displacement and velocity.

Finally, power analysis for both PEA and SEA was done using inverse dynamics. It showed that a decrease in torque stiffness from hardening to softening increases the power requirement of the system. A comparison between the PEA and SEA configuration showed that PEA required more power, thus for power considerations, SEA should be used.

## 7.1 Further Work

- Lyapunov exponents can be calculated for the various scenarios where chaos was observed to ensure that the behavior is indeed chaotic and just a very high periodic response.
- Research to ascertain why the extended model did not capture the same response behaviors.
- The Adams model can be extended to include all the components of the real system.
- Experiments can be performed to ascertain the effect of these nonlinear behaviors on the exoskeleton itself, i.e what happens when the system is working within the region of chaos?.
- Experiments can also be performed to know if and how the compliant joint improves the human interaction of the system.

# Bibliography

- Adams, 2019.** Msc Adams. *Adams Student Edition*, 2019. URL <https://www.mscsoftware.com/page/adams-student-edition>.
- Adams/View, 2018.** Adams/View. *Adams/View User's Reference Manual*. MSC Software, 1. ed. edition, 2018.
- Bai et al., July 2017.** S. Bai, S. Christensen and M. R. U. Islam. *An upper-body exoskeleton with a novel shoulder mechanism for assistive applications*. 2017 IEEE International Conference on Advanced Intelligent Mechatronics (AIM), pages 1041–1046, 2017. ISSN 2159-6255. doi: 10.1109/AIM.2017.8014156.
- Beckerle et al., 2016.** Philipp Beckerle, Tom Verstraten, Glenn Mathijssen, Raphaël Furnémont, Bram Vanderborght and Dirk Lefeber. *Series and Parallel Elastic Actuation: Impact of natural dynamics on power and energy consumption*. Mechanism and Machine Theory, 102, 232–246, 2016. doi: <http://dx.doi.org/10.1016/j.mechmachtheory.2016.04.004>.
- Brennan et al., 2008.** M.J. Brennan, I. Kovacic and A. Carrella and T.P. Waters. *On the jump-up and jump-down frequencies of the Duffing oscillator*. Journal of Sound and Vibration, 318, 250–1261, 2008. doi: <https://doi.org/10.1016/j.jsv.2008.04.032>.
- Christensen et al., 2019.** Simon Christensen, Shaoping Bai, Sajid Rafique, Magnus Isaksson, Leonard O'Sullivan, Valerie Power and Gurminder Singh Virk. *AXO-SUIT - A Modular Full-Body Exoskeleton for Physical Assistance*. Mechanisms and Machine Science, 66, 443–450, 2019.
- David Wagg, 2015.** Simon Neild David Wagg. *Nonlinear Vibration with Control: For Flexible and Adaptive Structures*. Springer International Publishing, 2. ed. edition, 2015.
- Ferris et al., 2019.** Daniel P. Ferris, Bryan R. Schlink and Aaron J. Young. *Robotics: Exoskeletons*. Reference Module in Biomedical Sciences, 2, 645–651, 2019. doi: <https://doi.org/10.1016/B978-0-12-801238-3.99906-9>.
- Gopuraa et al., 2016.** R.A.R.C. Gopuraa, D.S.V. Bandaraa, Kazuo Kiguchib and G.K.I. Mann. *Developments in hardware systems of active upper-limb exoskeleton robots: A review*. Robotics and Autonomous Systems, 75, 203–220, 2016. doi: <https://doi.org/10.1016/j.robot.2015.10.001>.
- Grimmer and Seyfarth, 2011.** Martin Grimmer and André Seyfarth. *Stiffness Adjustment of a Series Elastic Actuator in a Knee Prosthesis for Walking and Running: The Trade-off between Energy and Peak Power Optimization*. IEEE International Conference on Intelligent Robots and Systems (IROS), 2011. doi: <https://doi.org/10.1109/IROS.2011.6094467>.
- Ham et al., 2009.** Ronald Van Ham, Thomas G. Sugar, Bram Vanderborght, Kevin W. Hollander and Dirk Lefeber. *Compliant actuator designs*. Robotics & Automation Magazine, 2009. doi: <https://doi.org/10.1109/MRA.2009.933629>.

- Inman, 2006.** Daniel J. Inman. *Vibration with Control*. John Wiley and Sons Ltd, 1. ed. edition, 2006.
- Jazar, 2007.** Reza N. Jazar. *Theory of Applied Robotics Kinematics, Dynamics, and Control*. Springer Science+Business Media, LLC, 1. ed. edition, 2007.
- K. et al., 2002.** Zaki K., Noah S., Rajagopal K.R. and Srinivasa A. R. *Effect of Nonlinear Stiffness on the Motion of a Flexible Pendulum*. *Nonlinear Dynamics*, 12, 1–18, 2002. doi: <https://doi.org/10.1023/A:1017512317443>.
- Kapitaniak, 1990.** Tomasz Kapitaniak. *Analytical condition for chaotic behaviour of the duffing oscillator*. *Physics Letters A*, 144, 322–324, 1990. doi: [https://doi.org/10.1016/0375-9601\(90\)90133-9](https://doi.org/10.1016/0375-9601(90)90133-9).
- Li and Bai, 2019.** Zhongyi Li and Shaoping Bai. *A novel revoluted joint of variable stiffness with reconfigurability*. *Mechanism and Machine Theory*, 133, p. 720–736, 2019.
- Lumori et al., 01 2011.** Mikaya Lumori, Johan Schoukens and John Lataire. *Identification of Stiffness and Damping in Nonlinear Systems*. *Conference Proceedings of the Society for Experimental Mechanics Series*, 3, 2011. doi: 10.1007/978-1-4419-9834-7\_32.
- Malatkar et al., 2006.** Pramod Malatkar, Shaw Fong Wong, Troy Pringle and Wei Keat Loh. *Pitfalls An Engineer Needs To Be Aware Of During Vibration Testing*. *Electronic Components and Technology Conference*, 12, 1–18, 2006. doi: <https://doi.org/10.1109/ECTC.2006.1645918>.
- Murray et al., 1994.** R. M. Murray, Z. X. Li and S. S. Sastry. *A Mathematical Introduction to Robotic Manipulation*, 1994.
- Norton, 2012.** Robert L. Norton. *Design of Machinery: An Introduction to the Synthesis and Analysis of Mechanisms and Machines*. McGraw-Hill, 7. ed. edition, 2012.
- Onur Sert, 2019.** Ender Cigeroglu Onur Sert. *A novel two-step pseudo-response based adaptive harmonic balance method for dynamic analysis of nonlinear structures*. *Mechanical Systems and Signal Processing*, 130, 610–631, 2019. doi: <https://doi.org/10.1016/j.ymssp.2019.05.028>.
- Rao, 1995.** Singiresu S. Rao. *Mechanical Vibrations*. Addison-Wesley Publishing Company, 3. ed. edition, 1995.
- Rui-Lan et al., 2012.** Tian Rui-Lan, Yang Xin-Wei, Cao Qing-Jie and Wu Qi-Liang. *Bifurcations and chaotic threshold for a nonlinear system with an irrational restoring force*. *Chinese Physics, B*, 2012. doi: <https://doi.org/10.1088/1674-1056/21/2/02050>.
- Won Young Yang, 2005.** Tae-Sang Chung John Morris Won Young Yang, Wenwu Cao. *APPLIED NUMERICAL METHODS USING MATLAB*. John Wiley and Sons, Inc, 1. ed. edition, 2005.



- Yan et al., 2019.** L. J. Yan, Q. M. Shen, J. M. Qiao D. Yang and P. Datseris. *Kinematic and Dynamic Modeling and Analysis of a Lower Extremity Exoskeleton*. 16th International Conference on Ubiquitous Robots (UR), pages 625–630, 2019.
- Yu et al., 2011.** Jun Yu, Rongbo Zhang and Guojuan Jin. *Bifurcation and chaos in a perturbed soliton equation with higher-order nonlinearity*. PHYSICA SCRIPTA, 84, 2011. doi: <https://doi.org/10.1088/0031-8949/84/06/065004>.



# A | Trigonometric Identities

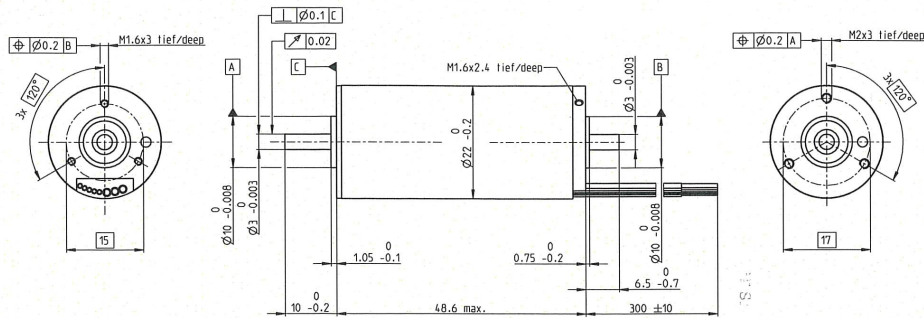
$$\begin{aligned} \sin^3(\omega t) &= \frac{1}{4} (\sin(\omega t) - \sin(3\omega t)) \\ \cos^3(\omega t) &= \frac{3}{4} (\cos(\omega t)) + \frac{1}{4} (\cos(3\omega t)) \\ F \sin(\omega t + \phi) &= a \sin(\omega t) + b \sin(\omega t) \\ F &= \sqrt{a^2 + b^2} \end{aligned} \tag{A.1}$$



# B | Data Sheet

270 x 0.586

## EC-4pole 22 Ø22 mm, brushless, 90 Watt High Power



M 1:1

- Stock program
- Standard program
- Special program (on request)

### Part Numbers

323217 323218 323219 323220 327739

### Motor Data

#### Values at nominal voltage

	V	18	24	36	48	48
1 Nominal voltage	V	18	24	36	48	48
2 No load speed	rpm	16300	16300	16300	16300	6900
3 No load current	mA	218	164	109	81.8	20.7
4 Nominal speed	rpm	14900	15000	14900	14900	5550
5 Nominal torque (max. continuous torque)	mNm	43.7	45.1	43.7	42.6	43.9
6 Nominal current (max. continuous current)	A	4.32	3.34	2.16	1.58	0.679
7 Stall torque	mNm	588	639	612	586	234
8 Stall current	A	55.8	45.5	29.1	20.9	3.55
9 Max. efficiency	%	88	89	88	88	85
<b>Characteristics</b>						
10 Terminal resistance phase to phase	Ω	0.323	0.527	1.24	2.3	13.5
11 Terminal inductance phase to phase	mH	0.0283	0.0503	0.113	0.201	1.11
12 Torque constant	mNm/A	10.5	14	21.1	28.1	66
13 Speed constant	rpm/V	907	680	453	340	145
14 Speed/torque gradient	rpm/mNm	27.8	25.5	26.7	27.9	29.7
15 Mechanical time constant	ms	1.61	1.48	1.55	1.62	1.72
16 Rotor inertia	gcm <sup>2</sup>	5.54	5.54	5.54	5.54	5.54

### Specifications

#### Thermal data

- 17 Thermal resistance housing-ambient 12.2 K/W
- 18 Thermal resistance winding-housing 1.19 K/W
- 19 Thermal time constant winding 5.12 s
- 20 Thermal time constant motor 482 s
- 21 Ambient temperature -20...+100°C
- 22 Max. winding temperature +155°C

#### Mechanical data (preloaded ball bearings)

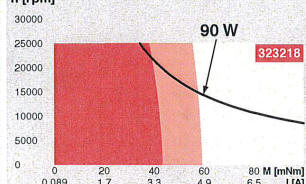
- 23 Max. speed 25000 rpm
- 24 Axial play at axial load < 3.0 N 0 mm
- 25 Radial play 0.14 mm
- 26 Max. axial load (dynamic) 4 N
- 27 Max. force for press fits (static) (static, shaft supported) 53 N
- 28 Max. radial load, 5 mm from flange 1000 N

#### Other specifications

- 29 Number of pole pairs 3
  - 30 Number of phases 3
  - 31 Weight of motor 125 g
- Values listed in the table are nominal.
- Connection motor** (Cable AWG 20)
- red Motor winding 1
  - white Motor winding 3
  - black Motor winding 2
- Connection sensors** (Cable AWG 26)
- red/grey Hall sensor 1
  - black/grey Hall sensor 2
  - white/grey Hall sensor 3
  - green V<sub>cc</sub> 5...24 VDC
  - blue GND
- Wiring diagram for Hall sensors see p. 45

### Operating Range

#### n [rpm]



- Continuous operation
- Continuous operation with reduced thermal resistance R<sub>th</sub> 50%
- Intermittent operation

Assigned power rating

### maxon Modular System

Details on catalog page 34

#### Planetary Gearhead

- 2 Ø22 mm
- 3 2.0 - 3.4 Nm

Page 343

#### Planetary Gearhead

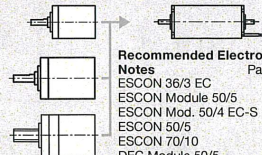
- Ø32 mm
- 1.0 - 6.0 Nm

Page 353

#### Screw Drive

- Ø32 mm

Page 382-387



#### Recommended Electronics:

Notes Page 27

ESCON 36/3 EC 455

ESCON Module 50/5 455

ESCON Mod. 50/4 EC-S 455

ESCON 50/5 457

ESCON 70/10 457

DEC Module 50/5 459

EPOS4 50/5 463

EPOS4 Mod./Comp. 50/5 463

EPOS2 P 24/5 470

MAXPOS 50/5 473

#### Encoder 16 EASY

128 - 1024 CPT, 3 channels

Page 418

#### Encoder 16 EASY XT

128 - 1024 CPT, 3 channels

Page 420

#### Encoder 16 EASY Absolute

4096 steps, Single Turn

Page 422

#### Encoder 16 EASY Absolute XT

4096 steps, Single Turn

Page 424

#### Encoder 16 RIO

1024 - 32768 CPT, 3 channels

Page 435

#### Encoder AEDL 5810

1024 - 5000 CPT, 3 channels

Page 438

#### Encoder HEDL 5540

500 CPT, 3 channels

Page 446

